Transfering spin into an extended π orbital of a large molecule

Taner Esat,[1,2,*] Thorsten Deilmann,[3] Benedikt Lechtenberg,[4] Christian Wagner,[1,2] Peter Krüger,[3] Ruslan Temirov,[1,2] Frithjof B. Anders,[4] Michael Rohlfing,[3] and F. Stefan Tautz[1,2]

[1]*Peter Grünberg Institute (PGI-3), Forschungszentrum Jülich, 52425 Jülich, Germany*

[2]*Jülich Aachen Research Alliance (JARA), Fundamentals of Future Information Technology, 52425 Jülich, Germany*

[3]*Institut für Festkörpertheorie, Westfälische Wilhelms-Universität Münster, 48149 Münster, Germany.*

[4]*Lehrstuhl für Theoretische Physik II, Technische Universität Dortmund, Otto-Hahn-Str. 4, 44221 Dortmund, Germany*

(Received 22 December 2014; revised manuscript received 12 March 2015; published 20 April 2015)

By means of low-temperature scanning tunneling microscopy (STM) and spectroscopy (STS), we have investigated the adsorption of single Au atoms on a PTCDA monolayer physisorbed on the Au(111) surface. A chemical reaction between the Au atom and the PTCDA molecule leads to the formation of a radical that has an unpaired electron in its highest occupied orbital. This orbital is a π orbital that extends over the whole Au-PTCDA complex. Because of the large Coulomb repulsion in this orbital, the unpaired electron generates a local moment when the molecule is adsorbed on the Au(111) surface. We demonstrate the formation of the radical and the existence of the local moment after adsorption by observing a zero-bias differential conductance peak that originates from the Kondo effect. By temperature dependent measurements of the zero-bias differential conductance, we determine the Kondo temperature to be $T_K = (38 \pm 8)$ K. For the theoretical description of the properties of the Au-PTCDA complex we use a hierarchy of methods, ranging from density functional theory (DFT) including a van der Waals correction to many-body perturbation theory (MBPT) and the numerical renormalization group (NRG) approach. Regarding the high-energy orbital spectrum, we obtain an excellent agreement with experiments by both spin-polarized DFT/MBPT and NRG. Moreover, the NRG provides an accurate description of the low-energy excitation spectrum of the spin degree of freedom, predicting a Kondo temperature very close to the experimental value. This is achieved by a detailed analysis of the universality of various definitions of T_K and by taking into account the full energy dependence of the coupling function between the molecule-metal complex and the metallic substrate.

DOI: 10.1103/PhysRevB.91.144415 PACS number(s): 75.20.Hr, 68.37.Ef, 73.20.Hb, 75.50.Xx

I. INTRODUCTION

Interest in magnetic properties of nanoscale structures has been growing rapidly for the last few years. Understanding and gaining control over their properties might open a route to nanospintronics and quantum computing [1]. Since molecular compounds demonstrate a remarkable tendency to self-assemble, the idea of combining the molecular pathway with magnetism is now attracting more attention [2,3]. Therefore it is crucial to obtain a better understanding of spin and charge transfer processes between molecules, surfaces, and even single atoms.

One of the interesting possibilities to tune the magnetic properties of molecules is by controlled charge transfer from other molecules or metal surfaces. For example, it has been shown that the electron-acceptor molecule TCNQ on a gold surface can be manipulated reversibly between two integer charge states by gating the local electric field with the tip of a scanning tunneling microscope and therefore inducing charge transfer from the adjacent donor molecule TMTFF [4]. A further example is provided by our previous work, in which we have demonstrated that the controlled cleavage of the π-conjugated molecule PTCDA from a Ag(111) surface gradually de-hybridizes the molecule from the metal substrate and tunes the molecule into a magnetic state, which then undergoes the Kondo effect with itinerant electrons in the metal [5–8].

Another interesting approach to adjust the magnetic properties of molecules is the on-surface chemical modification of individual molecules. Here, the reversible on- and off-switching of the Kondo resonance of a MnPc molecule through attachment and detachment of a single hydrogen atom [9] can be cited as an illustrative example. Also, a temperature-induced stepwise intramolecular ligand reaction of a gold adsorbed porphyrin molecule which induces changes in its magnetic fingerprint [10] falls in this category. Finally, it has been shown that the ligand and metal orbitals of metal phthalocyanines on a metal substrate can be selectively charged by site-dependent doping with one or more Li dopants [11].

In this work, we construct a metal-molecule complex that is a paramagnetic radical and in which, unlike in common molecular magnets where the spin usually resides in a d or f orbital of a metal ion that is shielded by organic ligands, the spin is carried by a π orbital that extends over the whole molecule. The advantage of such an extended radical lies in its propensity to interact magnetically with its neighbours, offering the potential to harness this coupling. In our experiments, we form chemically bonded metal-molecule complexes by reacting 3,4,9,10-perylene-tetracarboxylic dianhydride (PTCDA) molecules, adsorbed on the inert Au(111) surface, with single Au atoms. We investigate these Au-PTCDA complexes by means of scanning tunneling microscopy (STM). While the reversible bond formation of a single PTCDA molecule and an Au atom on a thin insulating film has been demonstrated before [12], we here investigate the Au-PTCDA complex on a metal substrate by scanning tunneling spectroscopy (STS). By demonstrating the Kondo effect, we prove that this metal-molecule complex indeed has an unpaired electron, which generates a local moment in the π orbital due to the

*Corresponding author: t.esat@fz-juelich.de

large Coulomb interaction compared to the electron-substracte coupling energy.

Complementary to our experimental investigation of this magnetic metal-molecule complex, we use density functional theory (DFT) including a van der Waals correction to calculate the structure of the Au-PTCDA complex, in excellent agreement with experiment, as revealed, for example, by calculated STM images. Furthermore, we use a spin-polarized DFT calculation plus many-body perturbation theory (MBPT) to obtain the high-energy charge excitation spectrum of Au-PTCDA complexes in the gas phase and adsorbed on Au(111). A correct physical description of the local moment formation and the Kondo effect, however, is not possible in a mean-field approach. Therefore, on top of these calculations, we finally perform numerical renormalization group (NRG) calculations to obtain the excitation spectrum of the metal-molecule complex on Au(111) also at low energies. Importantly, we use the full energy dependence of the coupling function between Au-PTCDA complex and the metal substrate as provided by the DFT/MBPT approach. This enables us to achieve a quantitatively correct description of its electronic properties, predicting a Kondo temperature within 1 K of the measured value and reaching a 0.25 eV accuracy of the high-energy spectrum.

II. METHODS

A. Experiment

An atomically clean Au(111) surface was prepared in ultrahigh-vacuum (UHV) by repeated cycles of Ar^+ sputtering and annealing at 430 °C, followed by a final annealing step at 180 °C for 30 minutes. Using a home-built Knudsen cell, we deposited a submonolayer film of PTCDA molecules onto a clean Au(111) surface held at room temperature. The sample was then transferred into a low-temperature CREATEC STM with a base temperature of $T = 9.5$ K. By heating a thin gold wire, we evaporated gold atoms onto the PTCDA submonolayer *in situ* at $T = 12$ K. The low sample temperature prevents clustering and single Au atoms are found on the sample after this processing step.

The electrochemically etched tungsten tip was treated in UHV by field emission and afterwards *in situ* by applying controlled voltage pulses and indentations into the clean gold surface until the spectroscopic signature of the Au(111) surface appeared. Differential conductance $dI/dV(V)$ spectra were recorded via the conventional lock-in technique with the feedback loop switched off.

The analysis of the Kondo effect requires recording differential conductance spectra at varying temperatures. After each temperature increase of the STM, we waited 20 h to obtain equilibrium conditions before recording the $dI/dV(V)$ spectra. Since broadening effects due to temperature and bias voltage modulation have a crucial influence on the linewidths of narrow peaks in scanning tunneling spectroscopy, it is essential to take these effects into account. Therefore the measured spectra were deconvoluted appropriately [13].

B. Theory

In addition to the experimental measurements, we have also studied the system theoretically, computing its geometrical and electronic structures. The geometrical structure was calculated with DFT, the electronic structure with DFT, MBPT, and NRG. While our DFT and MBPT methodologies are explained in this section, details regarding our NRG approach can be found in Sec. III D alongside its results.

1. Geometric structure

All DFT calculations concerning the structure are carried out in the framework of pseudopotentials using the SIESTA package [14–16]. The wave function is described by a double-zeta plus polarization basis (DZP) with s, p, and d orbitals included. We use five orbitals for H, 13 orbitals for C and O, and 15 orbitals for Au. The representation of quantities on meshes in reciprocal space is done with a cut-off energy of 250 Ry. For the $\vec{k}$ sampling of the freestanding layer, a 2×2 mesh in the two-dimensional Brillouin zone is used; if the surface is included, the sampling is increased to 4×6.

For determining the structure of a PTCDA monolayer on Au(111), the generalized gradient approximation (GGA) with the PBE functional [17] is used. Two issues have to be noted here: (1) since an incommensurate layer such as PTCDA/Au(111) cannot be treated with periodic boundary conditions, we have chosen for our calculations of PTCDA/Au(111) the commensurate unit cell in which PTCDA adsorbs on Ag(111) to obtain a system that can be treated within a supercell approach. On Ag(111), PTCDA forms a $(6,1,-3,5)$ superstructure that is nearly rectangular with a size of 18.83 Å × 12.52 Å. As a result, the angle between the lattice vectors is changed by 1° and their lengths are changed by −2.5% and +0.6% in comparison to the freestanding PTCDA monolayer. The two PTCDA molecules within the superstructure unit cell absorb at inequivalent sites. While one molecule is nearly aligned to the lattice underneath, the second one is turned by an angle of 16° relative to a high symmetry direction of the lattice. (2) Since the van der Waals interaction is crucial for weakly bound systems like organic molecules on metal surfaces, we include it in the formulation of Ruiz *et al.* [18] ($\mathrm{vdW^{surf}}$) for all structure optimizations. As a result of our PBE + $\mathrm{vdW^{surf}}$ calculation for PTCDA/Au(111) in the structure of PTCDA/Ag(111) we obtain an average height of $z_0 = 3.18$ Å for PTCDA on Au(111), in good agreement with the experimental value 3.27 Å [19]. The substrate is approximated by three Au layers with ideal atom positions. We employ this geometry for all calculations unless noted otherwise.

In order to determine the adsorption site of a single Au atom on a PTCDA monolayer, we employ a DFT calculation for a PTCDA layer that includes the interaction between PTCDA and the substrate by a model potential to facilitate the focussing on the adsorption of the single Au atom. This model potential consists of a harmonic potential between the Au surface and the C and O atoms, with potential parameters chosen such that the previously obtained physisorption height ($z_0 = 3.18$ Å) and elasticity ($\partial^2 E(z)/\partial z^2 = 8.4\,\mathrm{eV/Å^2}$ for the entire PTCDA molecule) result. The potential is then used for the C and O atoms to describe the interaction between Au-PTCDA and Au(111). For this calculation, the unit cell is taken from the (102) plane of the β-PTCDA bulk crystal [20], which contains two planar PTCDA molecules in a rectangular unit cell of

19.30 Å × 12.45 Å. To find the optimal adsorption site of the gold atom, the potential energy surface is evaluated on a dense mesh of (x,y) points above the PTCDA layer. The height of the Au atom and the coordinates of the PTCDA monolayer are optimized for all (x,y) positions of the atom until all forces are less than $10^{-4}\,\frac{\mathrm{Ry}}{a_\mathrm{B}}$.

2. *Electronic structure*

The calculation of STM images is performed at the level of the local density approximation (LDA) and within the Tersoff-Hamann approach [21], employing a spatial extrapolation of the wave function into the vacuum with additional empty orbitals [22] above the PTCDA monolayer for the Au-PTCDA/Au(111) structure mentioned above.

For further electronic properties, we employ a hierarchy of (spin polarized) DFT calculations (LDA, local density approximation, and LSDA, local spin density approximation),[1] many-body perturbation theory (MBPT) and numerical renormalization group (NRG) calculations. We perform spin-polarized DFT calculations to determine the mean-field electronic structure, as this provides us with an additional estimate of the Coulomb interaction U within the relevant orbital that leads to the magnetic moment of 1 μ_B on the molecule. Strictly speaking, of course, the intraorbital Coulomb interaction *cannot* be modeled as an effective single-particle potential, see Sec. III C 3 below.

The electronic properties of organic molecules in LDA and GGA(+vdW$^{\mathrm{surf}}$) are often nearly identical. Both functionals suffer from a distinct underestimation of the gap between the highest occupied molecular orbital (HOMO) and the lowest unoccupied molecular orbital (LUMO). We therefore apply MBPT to L(S)DA, by which a notable improvement is achieved, resulting in much more realistic quasiparticle (QP) energies. The MBPT replaces the XC potential of DFT by the self-energy operator, for which we employ the GW approximation [23].

Including the metal substrate in a GW calculation is, however, a formidable task. Therefore we use a perturbative L(S)DA+GdW approach introduced in Ref. [24] as a further approximation, which yields reliable QP energies by employing a model for the dielectric screening due to the substrate. Here L(S)DA+GdW labels the perturbative method to calculate QP corrections on top of L(S)DA by considering the change of the self-energy operator $\Delta\Sigma = iG(W - W_\mathrm{metal}) = iGdW$. Previous investigations employing this method for PTCDA on Ag(111) have shown good agreement with experiment (for details, see Ref. [7]). These calculations are carried out with a code implemented by ourselves [24,25]. Here, the representation of the wave function is done by atom-centered Gaussian orbitals with s, p, d, and s^* symmetry with several shells per atom [22,26].

The L(S)DA+GdW [24] approach employs dielectric model functions. For the PTCDA monolayer, these functions are explicitly evaluated on the basis of RPA results, while the screening due to the Au substrate is considered by an additional parametrized dielectric function. The L(S)DA+GdW calculation starts from the L(S)DA result for the freestanding monolayer in the commensurate structure and at the adsorption height from GGA+vdW (see Sec. II B 1) and builds up the dielectric function using both sets of model functions mentioned above. Thus, in the calculation of the QP corrections, the substrate is only included in terms of its dielectric polarization.

To calculate projected densities of state (PDOS), we follow the method described in Ref. [8]. In particular, three calculations have to be performed: in the first calculation the complete system, e.g., (Au-)PTCDA/Au(111), is investigated and we evaluate all energies E_n and the corresponding wave functions $|\Psi_n\rangle$ in L(S)DA. In the second calculation, the Au (111) surface is excluded and the wave functions $|\varphi_i\rangle$ for a few relevant states of the molecular (Au-)PTCDA monolayer (in the commensurate structure) are computed in L(S)DA. Finally, the third calculation is a repetition of the second one, but within L(S)DA+GdW in which the QP corrections Δ_i are determined; here, the Au(111) surface is incorporated in the form of model functions [8], as mentioned above. The spectrum of state $|\varphi_i\rangle$ in the full system is then given by its projected density of states, i.e.,

$$\rho_i(E-\Delta_i) = \sum_n |\langle\Psi_n|\varphi_i\rangle|^2 \delta(E - E_n - \Delta_i), \qquad (1)$$

in which the QP correction Δ_i is employed for the full system. If Δ_i is set to zero, i.e., many-body effects are neglected, the above equation reverts to the standard projection operation within L(S)DA.

The QP shift Δ_i also determines the filling of the orbital, according to

$$n_i = \int_{-\infty}^{E_F} \rho_i(E-\Delta_i)dE \qquad (2)$$

with $\rho_i(E)$ being the PDOS of orbital i resulting from the L(S)DA (i.e., $\Delta_i = 0$). The QP shift Δ_i, in turn, depends on the occupation of the orbital, i.e.,

$$\Delta_i = (1-n_i)\Delta_i^{n=0} + n_i\Delta_i^{n=1} + 2(n_i - n_\mathrm{LDA})U_i \qquad (3)$$

The intraorbital Coulomb repulsion in orbital i is calculated as

$$U_i = \int |\varphi_i(\vec{r})|^2 W(\vec{r},\vec{r}\,')|\varphi_i(\vec{r}\,')|^2 d^3r d^3r', \qquad (4)$$

were W is the screened Coulomb interaction (which also enters the GW self-energy). In Eq. (3), $\Delta_i^{n=0}$ and $\Delta_i^{n=1}$ denote the (fictitious) QP shifts for a completely empty ($n_i = 0$) or occupied ($n_i = 1$) orbital i, which can be obtained from L(S)DA+GdW calculations of the monolayer (in which the substrate is only considered in terms of its polarizability). For further details see Ref. [8].

NRG calculations allow to incorporate dynamical correlation effects and describe the Kondo effect. Because the NRG requires a rotationally invariant mean-field density of states, we use the LDA-GdW as its starting point. Details can be found in Sec. III D.

[1] We have convinced ourselves that in LDA as well as in generalized gradient approximation (GGA) the electronic structure of the bare Au(111) surface is in good agreement with the result of Ref. [50]

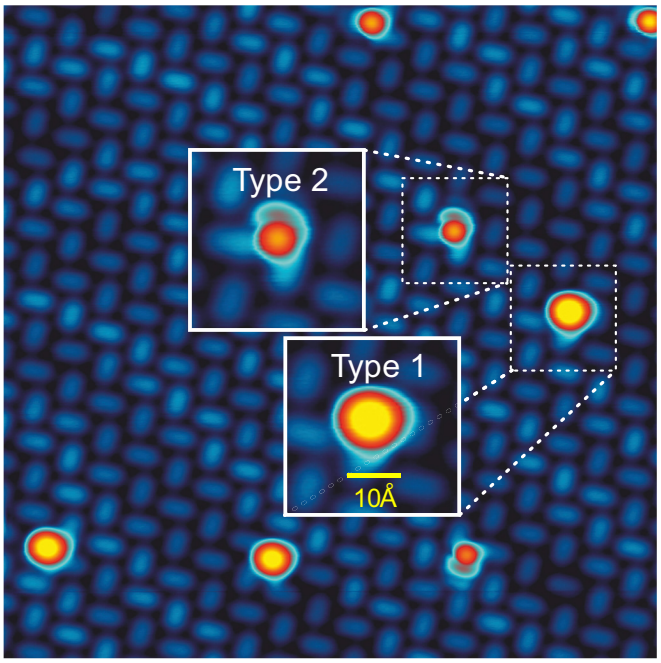

FIG. 1. (Color online) Constant current STM image (200 Å × 200 Å) after deposition of single Au atoms on a PTCDA monolayer on Au(111) (bias voltage $V = 50$ mV, tunneling current $I = 2.8 \times 10^{-11}$ A). In the insets the two observed types of Au-PTCDA complexes are shown.

III. RESULTS AND DISCUSSION

A. The Au-PTCDA complex and its structure

Figure 1 shows the PTCDA layer after deposition of Au atoms. The PTCDA molecules physisorb on the Au(111) surface and arrange into the so-called herringbone structure on Au(111). This structure is incommensurate and does not lift the herringbone reconstruction of the bare gold surface, as the brightness modulation of the PTCDA molecules in Fig. 1 clearly shows. On the PTCDA layer we observe two different types of features, both of which are related to single gold atoms. Type 1 complexes appear circular in the STM images and have a diameter of ∼10 Å. In contrast, type 2 complexes are smaller by a factor of ∼1.4 and in addition exhibit a halo next to the circular disk. Figure 2, in which differential conductance spectra of type 1 and type 2 complexes are displayed, clearly shows that the different sizes and shapes of both types go along with different spectral properties. While both types exhibit a sharp peak at zero bias, the remaining features indicate a very different electronic structure. Moreover, a closer look at the zero-bias peak reveals that the width and shape of this peak is well defined for type 1 complexes only [see also Fig. 7(b)], whereas both linewidths and lineshapes vary significantly among type 2 complexes (Fig. 3).

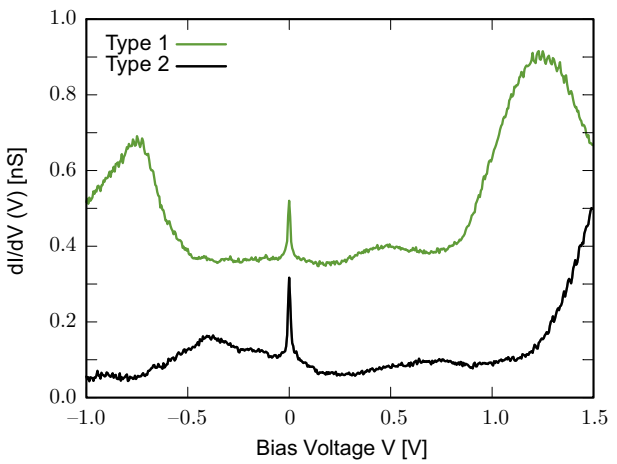

FIG. 2. (Color online) $dI/dV(V)$ spectra acquired over the center of type 1 (top) and type 2 (bottom) Au-PTCDA complexes. For clarity, the spectrum of type 1 is shifted by +0.5 nS (bias voltage and tunneling current at the stabilization point $V = 500$ mV and $I = 4.0 \times 10^{-11}$ A, lock-in modulation amplitude 5 mV at 713.3 Hz).

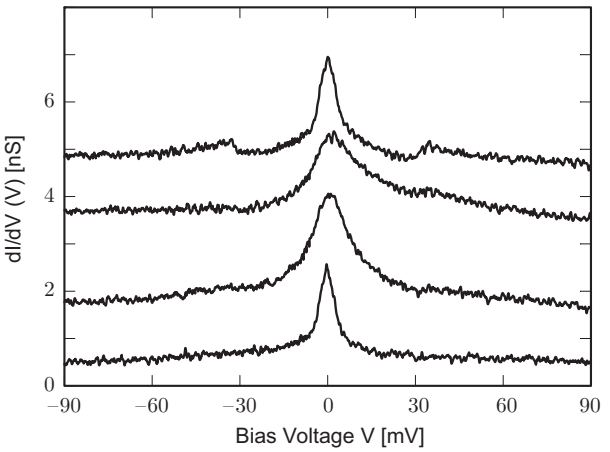

FIG. 3. $dI/dV(V)$ spectra acquired over the center of different type 2 complexes (bias voltage and tunneling current at the stabilization point $V = 360$ mV and $I = 2.5 \times 10^{-11}$ A, z-offset = +1.0 Å, lock-in modulation amplitude 1 mV at 5981 Hz). The spectra are vertically displaced for clarity.

To understand whether these differences in the electronic properties result from different Au adsorption positions in type 1 and type 2 complexes, we determine the precise positions of the Au atoms relative to the PTCDA layer. The analysis is carried out on the basis of large-scale high-resolution STM image (200 Å × 200 Å and 1024 pixel × 1024 pixel) by locating the centres of the respective circular disks in the PTCDA unit cell. Since the size and shape of the PTCDA unit cell is well known, we can correct the distortion of the measured high-resolution image by an affine homography. The resultant positions of the Au atoms are shown in Fig. 4(a). Because of the symmetry of the unit cell of the freestanding PTCDA layer, all data points can be displayed within one of its quadrants.[2] The figure reveals that the centres of both type 1 and 2 complexes are close to either of the two carbon atoms that are located midway along the long edges of the PTCDA molecule. Neglecting the environment, this allows for four equivalent adsorption positions on one PTCDA molecule.

[2]Although the surface breaks this symmetry, we neglect this effect because the monolayer is not adsorbed commensurately.

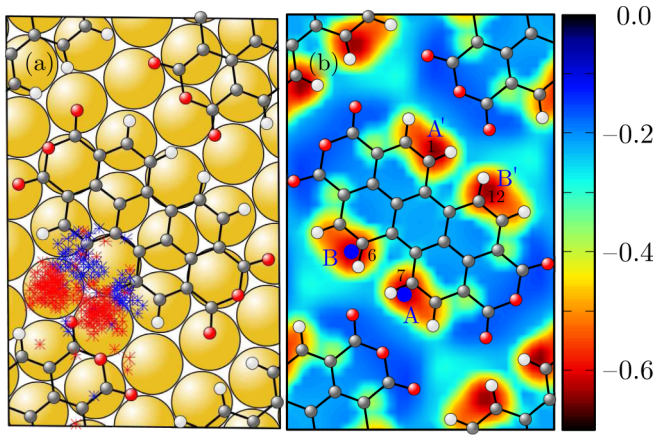

FIG. 4. (Color online) (a) Experimentally determined centres of type 1 (blue) and type 2 (red) Au atoms in the PTCDA unit cell on Au(111). The white, grey, and red circles indicate hydrogen, carbon, and oxygen atoms of PTCDA. The golden spheres denote the positions of the Au atoms in the topmost layer of the Au surface, assuming a commensurate arrangement of the molecules. (b) Potential energy surface (in eV) for an Au atom adsorbed on a PTCDA freestanding monolayer.

This experimentally observed adsorption site for Au atoms is also predicted by a DFT calculation for a PTCDA in which the interaction between PTCDA and the substrate is described by a model potential (see method Sec. II B 1 for details). The resulting potential energy surface for the Au atom on the PTCDA monolayer is shown in Fig. 4(b). Two nearly equivalent minima A and B with binding energies of 0.69 and 0.66 eV, respectively, are found. The potential energy above the center of a PTCDA molecule is approximately −0.25 eV. Remarkably, near the oxygen atoms the interaction with Au atoms nearly vanishes. Due to the symmetry of the monolayer there are four such minima per PTCDA molecule (A, A′, B, B′), i.e., eight minima per unit cell. At these minima, the Au atom is located above the C atoms labeled 1, 6, 7 or 12 of the perylene core, with a height of 2.1 Å above the monolayer and a distance of 2.2 Å to the nearest carbon atom. This bonding distance indicates the formation of a covalent bond between Au and PTCDA, in agreement with the finding in Ref. [12]. Hence, what at first sight appear to be Au atoms in Fig. 1 are in fact covalently bonded Au-PTCDA complexes. Obviously, their images are predominantly formed by the Au atom, which sticks out of the surface layer (cf. insets in Fig. 5).

To determine the influence of the metal substrate on the Au atom bonding, we have carried out a second set of calculations in which the topmost three layers of the Au(111) surface have explicitly been included. Although the PTCDA monolayer is therefore slightly deformed, the Au adsorption sites relative to the molecule stay the same as in the case of the freestanding layer. The binding energy in the minima, however, is larger (0.83 eV), due to the interaction with the surface. Essentially, the potential energy landscape for the freestanding layer is shifted rigidly by ∼0.15 eV to larger binding energies. The distance to the nearest carbon is again 2.2 Å, and the gold atom is located 5.4 Å above the topmost surface layer.

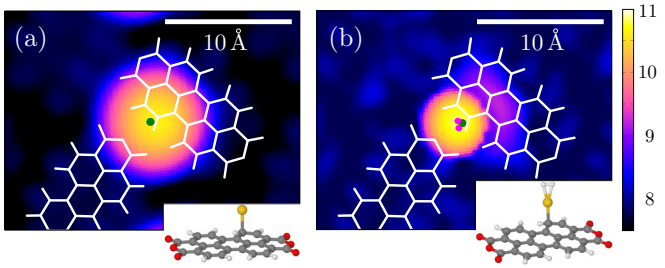

FIG. 5. (Color online) Theoretical constant current STM images of (a) Au on PTCDA/Au(111) and (b) Au on PTCDA/Au(111) with an additional hydrogen molecule adsorbed on the Au atom. The green circle denotes the position of the Au atom, the pink circles the positions of the hydrogen atoms. The tip height is given in angstrom. The insets below show the structure of the corresponding complexes.

We note that in Fig. 4(a) the STM image centers of type 2 complexes (red) are shifted by ∼1.5 Å from those of the type 1 complexes (blue) towards the gap between the molecules. At first glance, this might indicate a second adsorption site. However, such a site is not observed in our DFT calculations. The key to understanding the nature of type 2 complexes is their halo which appears in STM images (cf. Fig. 1). In Fig. 5(a), the simulated STM image of the covalently bonded Au-PTCDA complex is displayed. The image resembles experimentally observed type 1 complexes. If we add a hydrogen molecule in the calculation, both H atoms bind above the Au atom, in total with a binding energy of 0.35 eV. The distance between H and Au is 1.86 Å. If we now calculate the STM image of this complex adsorbed on the Au surface, a halo very similar to the one observed at type 2 complexes is found [Fig. 5(b)]. We therefore conclude that type 2 complexes in Fig. 1 most likely correspond to hydrogenated complexes.

This reasoning is corroborated by the observation that after a bake out of the low-temperature STM, which removes H_2 from the chamber, no type 2 atoms are observed any more (Fig. 6). The fact that in Fig. 4(a) the positions of type 2 complexes are slightly offset from type 1 complexes is an artefact of the site determination which does not take the different shapes of the two atoms types into account. Actually, comparing the simulated images in Fig. 5, it is evident that the center of the circular disk of type 1 complexes is located closer to the PTCDA molecule than the center of the (smaller) disk of type 2 complexes, in agreement with the experimental finding in Fig. 4(a).

Incidentally, the involvement of an additional H_2 molecule in type 2 complexes also explains the variability of their electronic structure (Fig. 3). In particular, the symmetric steps at $\simeq\pm30$ mV in some of the spectra are a strong indication of the presence of H_2. Those steps are known to derive from inelastic excitations. The observed frequency of $\simeq$30 meV fits well to translational [27,28] or rotational [29–33] modes of the hydrogen molecule.

B. Scanning tunneling spectra of the Au-PTCDA complex: Kondo effect

Having established the existence of covalently bonded Au-PTCDA complexes, we now study their electronic properties on the Au(111) surface. Thereby, we restrict our attention to

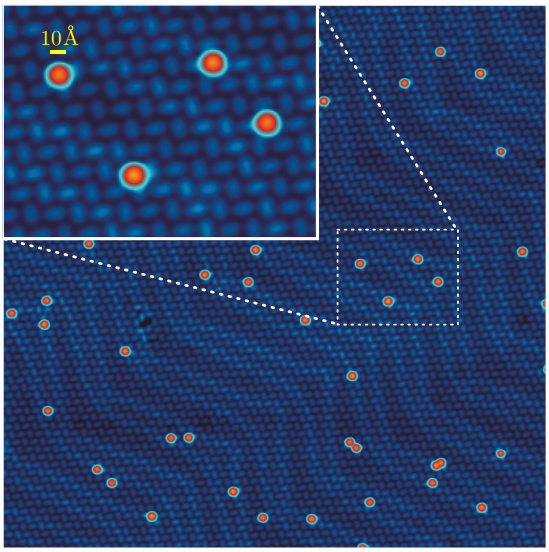

FIG. 6. (Color online) Constant current STM image (710 Å × 710 Å) taken after hydrogen decontamination of the low-temperature STM (bias voltage $V = 316$ mV, tunneling current $I = 2.5 \times 10^{-11}$ A). As highlighted in the inset, only type 1 Au-PTCDA complexes are observed.

type 1 (i.e., hydrogen-free) complexes. In the corresponding differential conductance spectrum in Fig. 2 we observe a peak at zero-bias voltage and three peaks at −0.8, +0.5, and 1.2 V. If we compare the peak at zero bias with the other peaks in the spectrum it is conspicuous that the former is much sharper and that it has a Lorentzian lineshape. This suggests that the zero-bias peak does not correspond to an electronic eigenstate of the Au-PTCDA complex. Since it is known from earlier work that charge transfer to the PTCDA molecule may bring forth the Kondo effect [5], and since the formation of the chemically bonded complex may well lead to such charge transfer and the formation of a radical, we conjecture that the zero-bias peak is in fact a Kondo resonance. This conjecture is corroborated by the analysis of its full width at half maximum (FWHM) and peak height [= zero-bias differential conductance $dI/dV(V = 0)$] as a function of temperature, as we will now show.

The extracted FWHM of the zero-bias peak are displayed in Fig. 7(a). The data show the expected temperature dependence for a Kondo resonance. We extract the Kondo temperature of the radical by fitting the expression [34]

$$\mathrm{FWHM} = \sqrt{(\alpha k_\mathrm{B} T)^2 + \left(2k_\mathrm{B} T_\mathrm{K}^{\mathrm{exp,FWHM}}\right)^2} \qquad (5)$$

to our data, with α and the Kondo temperature $T_\mathrm{K}^{\mathrm{exp,FWHM}}$ as fitting parameters. We find a Kondo temperature of $T_\mathrm{K}^{\mathrm{exp,FWHM}} = (30.7 \pm 1.0)$ K and $\alpha = (5.3 \pm 0.2)$, the latter of which is in good agreement with the theoretical value [35] of $\alpha = 5.4$.

In Fig. 7(c) the height of the zero-bias peak is plotted against the sample temperature. Here it is important to point out that the data points at all temperatures have been measured on the same Au atom and with the same tip. Moreover, for extracting heights of the zero-bias peaks that are directly comparable between the different temperatures, we always stabilize the tip above a PTCDA molecule at a fixed set point, before moving it above the Au-PTCDA complex at constant height and acquiring the differential conductance spectra there. Furthermore, we normalize all spectra to the same background differential conductance. Some spectra which were acquired with this method are shown in Fig. 7(d).

By using the empirical formula [36]

$$\frac{dI}{dV}(V = 0) = \frac{G_0}{\left[1 + \left(2^{1/s} - 1\right)\left(\frac{T}{T_\mathrm{K}^{\mathrm{zbc}}}\right)^2\right]^s} \qquad (6)$$

with $s = 0.22$ for a spin 1/2 system, we obtain from the data in Fig. 7(c) a Kondo temperature $T_\mathrm{K}^{\mathrm{exp,zbc}} = (38 \pm 8)$ K (zbc = zero-bias conductance) and $G_0 = (4.1 \pm 0.3)$ nS. Changing the distance between the tip and the Au-PTCDA complex does not affect the measured Kondo temperature. Within the error range, this value for $T_\mathrm{K}^{\mathrm{exp,zbc}}$ agrees well with the Kondo temperature which was extracted from the FWHM measurement series. However, we stress that there is no unique definition of the Kondo temperature and that different approaches to determine T_K may therefore lead to slightly different results. This will be discussed in more detail in Secs. III D 2 and III D 3 below. We can thus conclude that the Au-PTCDA complex is indeed a spin $\frac{1}{2}$ radical, and that this radical forms a Kondo ground state with the itinerant electrons of the metal substrate.

C. Electronic properties of the Au-PTCDA complex: density functional and many-body perturbation theory

Having proven that the Au-PTCDA complex undergoes the Kondo effect on the Au(111) surface, we now turn to a detailed analysis of the electronic properties of the molecule-metal complex. To this end, we carry out many-body perturbation calculations that are based on the spin-polarized local density approximation to density functional theory. Initially, we consider both PTCDA and the Au-PTCDA complex in the gas phase. We then turn to a PTCDA/Au(111) monolayer and finally to a monolayer in which one of the two PTCDA molecules carries an Au atom.

TABLE I. Energies (in eV) for the gas-phase PTCDA and Au-PTCDA in L(S)DA, GW, and L(S)DA+GdW measured with respect to E_Vac. In contrast to the results for PTCDA (top, calculated in LDA) those of the open-shell Au-PTCDA complex (bottom) are spin polarized. Due to the odd number of electrons, the LUMO+Au state is half-filled. For the nomenclature of the states of the Au-PTCDA complex see Table II and Fig. 8.

Level	L(S)DA	GW	L(S)DA+GdW
HOMO	−6.15	−7.35	−7.82
LUMO	−4.71	−2.75	−3.01
LUMO+1	−3.39	−1.15	−1.31
Gap	1.44	4.60	4.81
HOMO+Au	−7.25, −7.22	−8.44, −8.32	−8.92, −8.72
LUMO+Au	−6.37, −6.25	−7.36, −4.33	−7.77, −4.50
LUMO−Au	−5.46, −5.39	−3.60, −3.36	−3.87, −3.50
LUMO+1	−4.37, −4.34	−2.37, −2.28	−2.52, −2.44
Gap	0.12	3.03	3.27

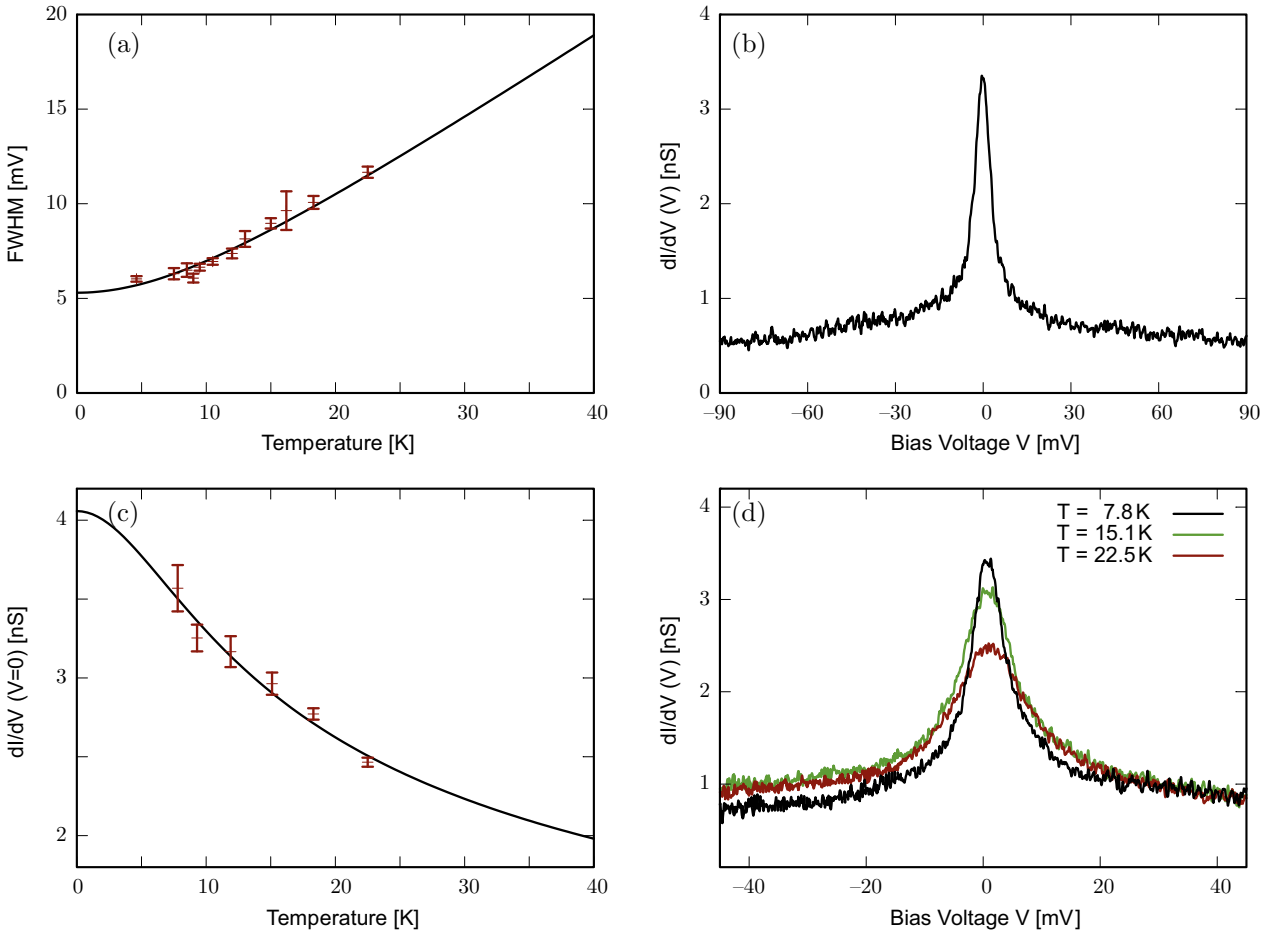

FIG. 7. (Color online) (a) FWHM of the differential conductance peak at zero bias, measured at different temperatures. Data points include measurements with different tips and on different Au-PTCDA complexes of type 1. Note that the FWHM after deconvolution to correct for broadening due to finite temperature and modulation amplitude are plotted. (b) $dI/dV(V)$ conductance (as measured, not deconvoluted) of one type 1 Au-PTCDA at $T \approx 5$ K. (c) Peak heights of the differential conductance peak at zero bias, measured at different temperatures. All data points were measured with the same tip on the same Au-PTCDA complex. (d) $dI/dV(V)$ conductance of the same radical as in (c) at specific temperatures. (b) and (d) Bias voltage and tunneling current at the stabilization point $V = 316$ mV and $I = 2.5 \times 10^{-11}$ A, z offset $=$ $+1.0$ Å, lock-in modulation amplitude 1 mV at 6100 Hz.

1. Gas-phase molecules

We start with the isolated PTCDA molecule. This system has been investigated experimentally and theoretically in detail by Dori *et al.* [37]. We have performed calculations within LDA, the GW approximation and the simplified LDA+GdW method for this system. In the top part of Table I the energies for a single PTCDA molecule are listed. We note that replacing the LDA by the LSDA for isolated PTCDA yields the same result, due to its closed-shell singlet ground state. For PTCDA, a HOMO-LUMO gap of only 1.4 eV is observed in LDA. Using the GW approximation, the HOMO is shifted -1.2 eV downward, while the LUMO is moved almost $+2$ eV upward from the LDA value. This leads to a gap of 4.6 eV (compared to 4.9 eV in Ref. [37]). Compared to the GW approximation, in LDA+GdW the HOMO is moved downward slightly more, while the LUMO is moved upward less strongly; the gap, although moderately increased to 4.8 eV, is still in good agreement with the GW approximation. Similarly, the LUMO+1 state is shifted upward by $+2.2$ eV (GW) or $+2.1$ eV (LDA+GdW) with respect to LDA.

Next, we consider the gas-phase Au-PTCDA complex. The isosurfaces of its frontier wave functions are shown in Fig. 8 in comparison with those of the free PTCDA molecule. The LUMO of bare PTCDA hybridizes strongly with the Au 6s level, forming a bonding (LUMO+Au) and an antibonding (LUMO$-$Au) combination. Table II reveals that in addition

TABLE II. Orbital composition of the three most important states of the gas-phase Au-PTCDA complex in terms of projection amplitudes onto states of the Au atom (6s,6p) and the PTCDA molecule (HOMO, LUMO, LUMO+3). The states of the Au-PTCDA complex are labeled according to their dominant character as HOMO+Au, LUMO+Au, and LUMO$-$Au. Only the most significant contributions are listed.

	Au_{6s}	Au_{6p}	HOMO	LUMO	LUMO+3
HOMO+Au	0.14	0.00	0.74	0.01	0.00
LUMO+Au	0.29	0.07	0.16	0.31	0.03
LUMO$-$Au	0.12	0.07	0.01	0.64	0.07

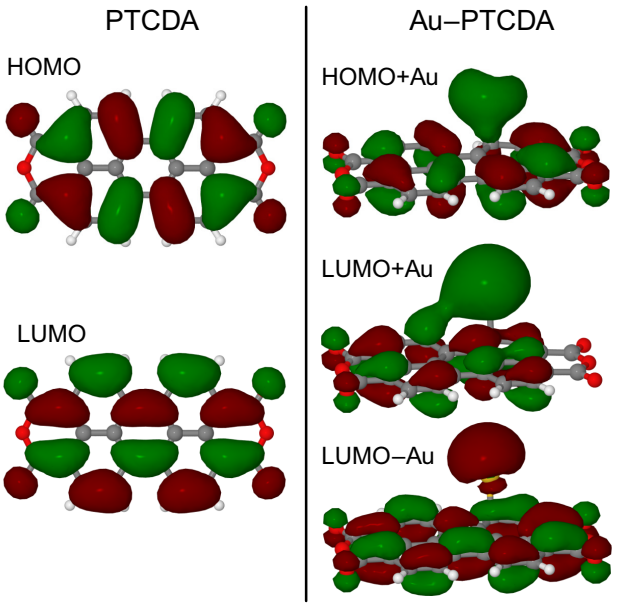

FIG. 8. (Color online) Wave functions of PTCDA (left) and Au-PTCDA (right) for orbitals around E_F calculated within LDA. Green indicates the positive isosurface, red the negative one.

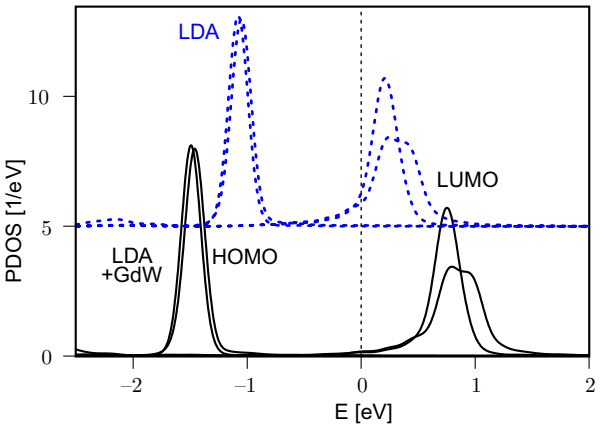

FIG. 9. (Color online) Projected density of states of a commensurate PTCDA monolayer adsorbed on Au(111) with two PTCDA molecules in the unit cell. The PDOS was obtained within the LDA (dashed blue, vertically shifted for clarity) and the LDA+GdW (black). The energies are given relative to the Fermi level of the Au(111) substrate.

to the Au 6s level, the PTCDA HOMO and PTCDA LUMO states, also the Au 6p and the PTCDA LUMO+3 contribute to the frontier orbitals of the Au-PTCDA complex (The numbers in each line of Table II do not sum up to one, because many other states contribute to a smaller extent). The most notable observation reported in Table II is that there is a sizable admixture of the PTCDA HOMO into the bonding combination of LUMO and Au 6s.

The Au-PTCDA complex has an odd number of electrons (Au $6s^1$). Hence its highest occupied level is half filled. This turns out to be the LUMO+Au state. Within LSDA, all Au-PTCDA levels are spin split by only ∼0.1 eV (see Table I). However, the GW approximation gives similar QP corrections for the Au-PTCDA complex as for the pure PTCDA. In particular, it opens a gap of 3.0 eV between the LUMO + Au ↑ and LUMO + Au ↓ states. This is a consequence of the fact that the orbital is half-filled and its two spin channels are separated by the Coulomb interaction U. The physical significance of the splitting will be further discussed below (Sec. III C 3) [38]. Note that for empty or doubly occupied orbitals such as HOMO+Au, LUMO−Au, or LUMO+1, QP corrections do not affect the spin-splitting significantly. For example, the fully occupied HOMO+Au state shifts down by more than −1 eV, while the unoccupied levels are moved up by +2 eV.

2. *PTCDA on the Au(111) surface*

In the following, we discuss the PTCDA monolayer on Au(111), which we model as a commensurate monolayer in order to be able to apply periodic boundary conditions (see Sec. II B 1 for more details). In DFT-LDA as well as DFT-GGA, we obtain nearly identical spectra for the monolayer, which, however, deviate strongly from the experimental finding that on Au(111) the PTCDA LUMO is not occupied [39].[3] Therefore we once again turn to the LDA+GdW approach, which has produced very realistic spectral results for the gas-phase PTCDA (see Table I) and for PTCDA/Ag(111) [7].

In Fig. 9, the corresponding PDOS as calculated in LDA and LDA+GdW is shown. Again, replacing LDA by LSDA in these calculations gives the same result, without spin-splitting. The two inequivalent adsorption sites in the commensurate unit cell (see Sec. II B 1) lead to different spectral line shapes of the PTCDA LUMO, with a stronger broadening for the PTCDA molecule that is aligned to the Au(111) lattice. The figure clearly illustrates the QP corrections as shifts of the corresponding peaks between the LDA and the LDA+GdW spectra (−0.4 eV for both HOMO peaks at −1.5 and −1.45 eV, and +0.5 eV for both LUMO peaks at 0.75 and 0.9 eV). Note that only the QP corrections lead to the prediction of the LUMO as being nearly empty (while in LDA the LUMO is occupied by 0.3 electrons), in agreement with the experimental finding.

As a consequence of the QP shifts, the HOMO-LUMO gap increases from 1.3 eV in LDA to 2.2 eV in LDA+GdW (Fig. 9). We note that for a PTCDA monolayer calculated in the same unit cell as considered here for PTCDA/Au(111) but *without* substrate, the QP shifts are distinctly larger (−1.0 for the HOMO and +1.1 eV for the LUMO). This can be explained by the absence of substrate screening. Yet, the HOMO-LUMO gap of this free-standing PTCDA monolayer (3.4 eV) is still smaller than the one of gas-phase PTCDA molecules (4.8 eV). Although the PTCDA molecules are only weakly bound through hydrogen bridges, they contribute environmental polarizability and this leads to a decreased gap. On the other hand, placing a *single* PTCDA molecule on the metal surface leads to a gap of 2.6 eV, showing that, as expected, the increase of the environmental polarizability by the metallic Au(111) substrate is much stronger than by adjacent molecules. Nevertheless, we

[3]We have performed calculations with six layers of Au instead of three. The charge transfer is the same as for three Au layers.

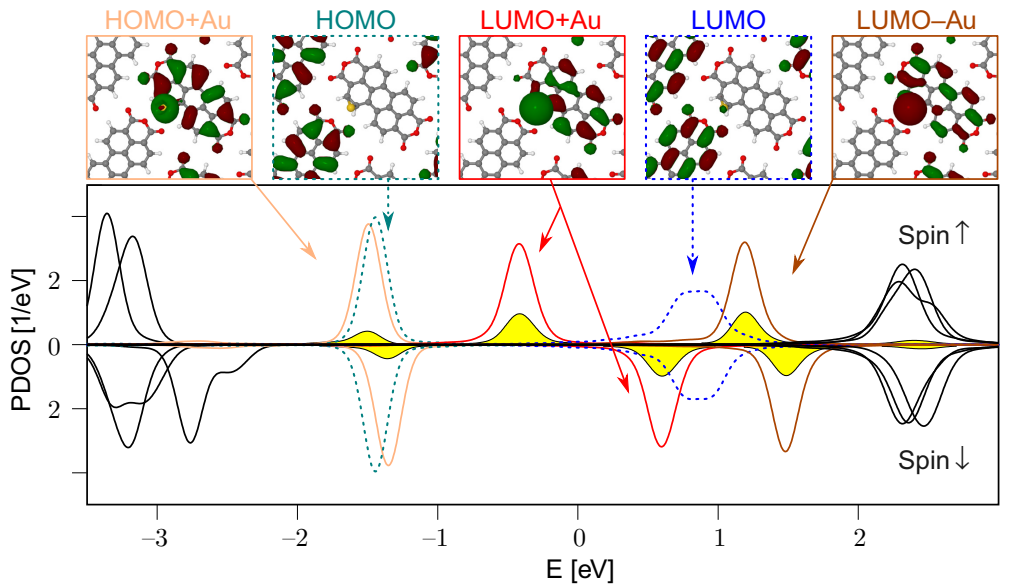

FIG. 10. (Color online) Projected density of states for the PTCDA molecule and the Au-PTCDA complex in the monolayer, adsorbed on Au(111). The PDOS was evaluated from LDA+GdW energies. The projection on the states of the Au-PTCDA complex is shown in shades of red (solid), while projections on the PTCDA molecule are shown in shades of blue (dashed). The yellow curve marks the projection on the states of the Au atom (6s and 6p) only. In addition the wave functions of some of the involved levels are plotted in corresponding colors. The energies are given relative to the Fermi level of the Au(111) substrate.

can conclude that both neighboring molecules and the Au(111) surface are instrumental for reducing the HOMO-LUMO gap below the value of the free molecule. Clearly, the effects of the metal substrate and the molecular environment on the gap are not additive.

3. *Au-PTCDA on the Au(111) surface*

Next, we perform spin-polarized electronic structure calculations (LSDA+GdW) for the Au-PTCDA complex adsorbed on the Au surface, in order to simulate the effect of the local Coulomb interaction in the LUMO+Au orbital at the mean-field level. While this treatment, which implies a rigid spin orientation, cannot describe the spin degree of freedom and thus fails to predict the correct low-energy spectrum [38], it can be used to gain insight into the high-energy spectrum that is dominated by the electronic degrees of freedom. Again a commensurate unit cell is employed, as discussed in the Sec. II B 1, with one PTCDA molecule and one Au-PTCDA complex per unit cell.

In Fig. 10, the LSDA+GdW projected density of states of this system is shown. The unit cell contains two PTCDA molecules, with an Au atom attached to one of them. Concomitantly, the system exhibits five molecular states in the energy range of Fig. 10, i.e., the HOMO and LUMO of the bare PTCDA, as well as HOMO+Au, LUMO+Au and LUMO−Au of Au-PTCDA. All states occur as spin-up and as spin-down. The projection onto the bare PTCDA molecule (blue) shows the HOMO at an energy of −1.6 eV (QP correction: −0.4 eV) and the LUMO at 0.8 eV (QP correction: +0.5 eV). Both levels are nearly spin-degenerate, confirming the expectation that the physics of PTCDA (cf. the discussion of the pure PTCDA/Au(111) monolayer in the previous Sec. III C 2) is not changed by a neighboring Au-PTCDA complex.

Regarding the projections onto the Au-PTCDA complex (red), we observe two types of behavior: on the one hand, the HOMO+Au of the Au-PTCDA complex is located at essentially the same energy as the HOMO of bare PTCDA, with a minor spin-splitting of 0.15 eV only, which is caused by slightly different QP corrections of −0.40 and −0.55 eV for spin-up and spin-down electrons, respectively. On the other hand, the LUMO-derived states of the Au-PTCDA complex show a strong spin splitting, amounting to 1.1 eV for the bonding LUMO+Au and 0.3 eV for the antibonding LUMO−Au orbital. As for the gas-phase complex, these splittings arise from quasiparticle corrections (−0.4 eV for the LUMO+Au ↑, +0.7 eV for the LUMO+Au ↓, +0.5 eV for the LUMO−Au ↑, and +0.8 eV for the LUMO−Au ↓). Because of the large splitting, only the spin-up state of the LUMO+Au orbital is found below the Fermi energy. The LUMO+Au is therefore a singly occupied molecular orbital (SOMO) with a nearly fully occupied majority spin state at −0.5 eV and a nearly empty minority spin state at 0.6 eV. Integrating the PDOS, we find that the LUMO+Au orbital is occupied with about one electron ($n = 0.5$).

Comparing the theoretical spectrum in Fig. 10 to the experimental spectrum in Fig. 2, it is tempting to assign the state measured at −0.8 eV to the LUMO+Au ↑ (theoretical value −0.5 eV) and the state measured at 0.5 eV to LUMO+Au ↓ (theoretical value 0.6 eV). The strong peak measured at 1.2 eV can be ascribed to a superposition of both spin channels of the antibonding LUMO−Au (theoretical values 1.2 and 1.5 eV). The latter assignment is consistent with the larger experimental FWHM of this peak (0.5 eV) as compared to the other electronic levels in the spectrum.

These assignments are further supported by the fact that all levels in the range −2.0 to +1.5 eV have in the calculation a substantial projection on the states of the Au atom (shown

in yellow in Fig. 10). This is a prerequisite for being able to see these states in STS spectra, because in experiment the spectrum is measured when the tip is above the Au atom and thus states localized there are approximately 2 Å closer to the tip than those localized on PTCDA. Because the wave function decreases roughly by one order of magnitude per angstrom [22], states without a contribution from Au are reduced in amplitude by two orders of magnitude and are expected to be invisible.

We note that the spin-splitting between LUMO + Au ↑ and LUMO + Au ↓ that is obtained in LSDA+GdW for Au-PTCDA on Au(111) is substantially smaller than the corresponding value of 3.27 eV in the gas-phase complex (Table I). As discussed in the previous Sec. III C 2 for the PTCDA molecule, the reduction of the gap is caused by the increased environmental polarizability, both due to the Au(111) surface and the surrounding PTCDA molecules and Au-PTCDA complexes.

The LSDA+GdW calculation can be used to evaluate the Coulomb repulsion U in the LUMO+Au orbital, using Eq. (4). This yields a value of 1.3 eV for the Au-PTCDA complex in a mixed PTCDA/Au-PTCDA monolayer on Au(111). In first order, this Coulomb repulsion can also be obtained as the energy difference between the fully occupied LUMO + Au ↑ and the completely empty LUMO + Au ↓ orbital. Note, however, that this difference (1.1 eV) is slightly smaller than the U obtained from Eq. (4). The origin of this discrepancy are QP renormalizations. The single-particle spectrum therefore shows an effective U. We will observe a similar behavior for the NRG calculation (see Sec. III D 1).

Next, we would like to include the low-energy region of the spectrum in Fig. 2 (i.e., the energy range around the Fermi level at $E = 0$) into our consideration. As mentioned above, this requires explicit accounting for the U-induced dynamical intraorbital correlations that create the spin degree of freedom. Moreover, the local spin scatters the conduction electrons, which in turn leads to a screening of the local moment that is characteristic of the Kondo ground state whose spectral signature can be found in the low-energy part of Fig. 2.

The dynamical correlations can be taken into account by performing an NRG calculation. In the present case, we use realistic input parameters for the level position of the LUMO+Au state (taken from the MBPT spectral function), its intraorbital Coulomb repulsion [taken, e.g., from Eq. (4)], and the coupling between the electrons in LUMO+Au state and the conduction electrons (taken from MPBT). However, the spin-polarized calculation is not feasible for this purpose. For a spin-rotationally invariant solution, we have to resort to a starting point given by an *unpolarized* LDA+GdW calculation.

The spectral function resulting from the LDA+GdW calculation is shown in the middle of Fig. 11, in comparison to the corresponding function from the LSDA+GdW at the top (replotted from Fig. 10). As expected from the partial occupancy of the LUMO+Au state in the spin-polarized calculation, the LUMO+Au level is found around the Fermi energy in the unpolarized calculation. Its occupancy can be calculated by Eqs. (2) and (3) from the quasiparticle shifts for fictitious zero/complete occupation ($\Delta^{n=0} = +0.64\,\text{eV}/\Delta^{n=1} = -0.37\,\text{eV}$), the filling within LDA ($n_{\text{LDA}} = 0.68$), and the Coulomb interaction U, which is

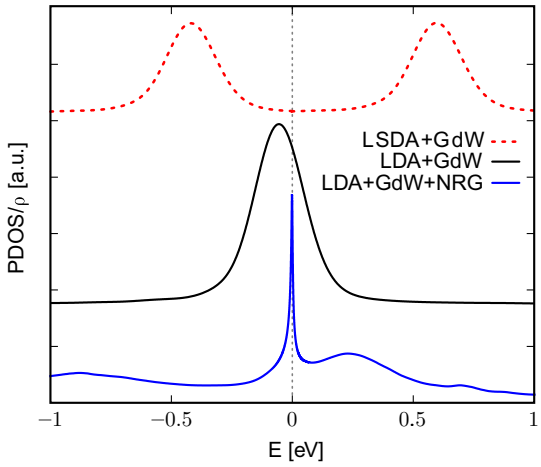

FIG. 11. (Color online) Projected density of states of the LUMO+Au orbital from an unpolarized LDA+GdW calculation (black) in comparison to the spin-polarized LSDA+GdW result (red dashed) of Fig. 10. In addition, the LDA+GdW+NRG result is included ($T = 0\,\text{K}$ and $U = 1.2\,\text{eV}$, see Sec. III D).

calculated according to Eq. (4) and amounts to $U = 1.3\,\text{eV}$ for this unpolarized calculation. We find a resulting occupation of $n = 0.71$ and an overall QP correction of $\Delta^{GdW} = -0.01\,\text{eV}$. We note that it is purely coincidental that we obtain a nearly negligible QP shift for the present situation.

Before turning to the NRG calculations and their detailed analysis in the next Sec. III D, we comment on the accuracy of the input parameters to the NRG, which are taken from LDA+GdW. First of all, there are structural uncertainties: a commensurate PTCDA monolayer is used in our DFT calculations, while point-on-line epitaxy is observed for PTCDA/Au(111) in experiment, and we find slightly different adsorption heights of PTCDA in our GGA + vdW$^{\text{surf}}$ calculation as compared to experiment (difference of the order 0.1 Å). Clearly, this may also influence the level positions with respect to the Fermi energy of the substrate, both for the bare PTCDA molecule and evidently also for the Au-PTCDA complex. We estimate this uncertainty to be of order 0.2 eV. Furthermore, the accuracy of GW and LDA+GdW calculations depends on the starting point (Hartree-Fock, LDA, ...). We use a scissor operator to anticipate the opening of the gap and therefore to reduce this dependency. The scissor operator is applied to the LDA spectrum before calculating G, W and thus Σ. This procedure approximately anticipates the finally resulting QP shifts and accelerates their self-consistent determination. Note that different QP shifts are obtained for all individual states. Nevertheless, errors of the QP corrections in GW cannot be reduced to less than 0.1 eV. The error of LDA+GdW is expected to be of the same size. As a consequence of these inaccuracies, and additionally because a finite $\vec{k}$ point mesh and a finite broadening for the calculation of the PDOS have been employed, we cannot exclude an uncertainty of $\Delta n = 0.05$ in the occupation of LUMO+Au state. This will affect the level position ϵ_0 and the hybridization in the same order. Finally, the Coulomb repulsion U slightly differs for different Au atom positions in the unit cell (positions A, A′, B, B′ in Fig. 4) in the range of 0.1 eV.

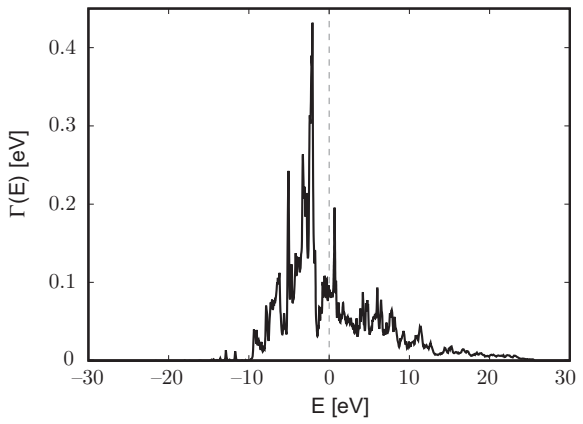

FIG. 12. The full energy-dependent hybridization function $\Gamma(E)$ obtained from the LDA+GdW PDOS. $\Gamma(E)$ is independent of the Coulomb interaction U and therefore always the same for every NRG calculation in which an energy-dependent hybridization function is used.

D. Electronic properties of the Au-PTCDA complex: Numerical renormalization group

1. Combining the LDA+GdW and the numerical renormalization group

We now discuss NRG calculations to incorporate dynamical correlation effects into the spectrum of the Au-PTCDA complex on the Au(111) surface. We employ the procedure outlined in Ref. [8]. In this approach, the LDA+GdW result is mapped onto a single-orbital Anderson model, which is then solved using the NRG approach, in order to incorporate the Kondo effect that is experimentally observed in the type 1 dI/dV spectrum of Fig. 2. Because only the LUMO+Au state shows a significant contribution to the spectral function around E_F, a single-orbital Anderson model is used to model the dynamical coupling of the LUMO+Au orbital to the substrate.

By treating the projected DOS obtained by the LDA+GdW as an effective mean-field spectrum $\rho_{GdW}(E)$, we are able to extract the bare level position ϵ_0 and the complex coupling functions $\Delta(E)$ between the Au-PTCDA complex and the substrate by equating

$$\rho_{GdW}(E) \equiv \lim_{\delta\to 0^+} \Im \frac{1}{\pi} \frac{1}{E - i\delta - \epsilon_0 - nU - \Delta(E - i\delta)}. \quad (7)$$

Here, U denotes the estimated intraorbital Coulomb interaction, and n the occupation number of the energy level consistent with $\rho_{GdW}(E)$. Since the LDA+GdW and LSDA+GdW predict slightly different values of U (see discussions above), we take U as a model parameter and vary the interaction within the predicted bounds: the LDA+GdW gives $U = 1.3$ eV and an occupancy $n = 0.71$, while the LSDA+GdW spectrum with an occupation of $n = 0.50$ yields $U = 1.1$ eV. The parameters U, ϵ_0 and the complex function $\Delta(z)$ enter an NRG [40,41] calculation, where $\Gamma(E) = \lim_{\delta\to 0^+} \Im\Delta(E - i\delta)$ defines the hybridization strength between the Au-PTCDA complex and the substrate. As we will see below, it is crucial to retain the *full energy dependence* of the hybridization function $\Gamma(E)$, which is plotted in Fig. 12, in our NRG calculation. Following Eq. (7), we find that ϵ_0 ranges from $\epsilon_0 = -0.88$ eV for $U = 1.1$ eV, $\epsilon_0 = -0.95$ eV for $U = 1.2$ eV to $\epsilon_0 = -1.02$ eV for $U = 1.3$ eV.

The resulting NRG spectrum for $U = 1.2$ eV (lower curve of Fig. 11) indeed shows the Kondo peak and two charge excitation peaks at -0.9 and 0.2 eV. The latter correspond to the two LUMO + Au $\uparrow$ and LUMO + Au $\downarrow$ levels of the spin-polarized LSDA+GdW mean-field spectrum at the top of Fig. 11 (located at -0.45 and 0.55 eV). Note that the charge excitation peaks of the NRG are shifted nearly rigidly with respect to the ones of the LSDA+GdW; in fact, they are found reasonably close to the *experimental* positions (-0.8 and 0.5 eV). The NRG calculation and experiment thus agree in showing a more particle-hole asymmetric situation than the LSDA+GdW calculation. Given the uncertainties of the input parameters into the NRG, a correspondence with experiment regarding the charge excitations to within 0.25 eV is an excellent result, showing that our modeling is describing the system at a quantitative level. Similar to the LSDA+GdW, we also observe in the NRG a slight reduction of the "effective U," defined as the difference between the two charge excitation peaks (1.1 eV for the spectrum in Fig. 11), below the input value going into the calculation (1.2 eV).

To illustrate the effect of the above mentioned uncertainty of the input parameter U, NRG spectra of the LUMO+Au state on Au(111) are shown in Fig. 13(a) for different interactions U and $T = 5$ K. With increasing interaction U one observes a narrowing of the Kondo peak and thus a decreasing of the Kondo temperature as expected from the analytical estimate of the Kondo temperature stated in Eq. (10) below.

We finally note in passing that for half-filling and absent orbital-substrate interaction the spin-polarized LSDA+GdW spectrum after averaging over the two spins and the high-energy part of NRG spectrum in Fig. 11 would be qualitatively very similar. Moreover, the local moment approach of Glossop and Logan [42] uses the spin-polarized mean-field solution as starting point: first, the mean-field spectrum is symmetrized to restore the rotational invariance in the spin space and then the missing Kondo resonance is calculated by including the low-energy two-particle corrections of a random phase approximation.

2. Results for the Kondo temperature

We now turn to a detailed analysis of the Kondo temperatures resulting from the NRG calculations. Since the Kondo temperature depends extremely sensitively on the physical parameters (molecule-metal coupling, energy level position, and Coulomb interaction), the comparison of the LDA+GdW+NRG-predicted to the experimental Kondo temperature is a very sensitive gauge of the accuracy of our first-principles DFT/MBPT analysis.

Since the Kondo energy scale is a crossover rather than a transition scale, there is, however, no unambiguous definition of the Kondo temperature. We therefore employ three different approaches to obtain the Kondo temperature, namely, (a) a fit to the T dependence of the zero-bias conductance, which should be a universal function of T/T_K. This leads to a Kondo temperature which we denote by T_K^{zbc} (zbc = zero-bias conductance). (b) The evaluation of the analytic formula

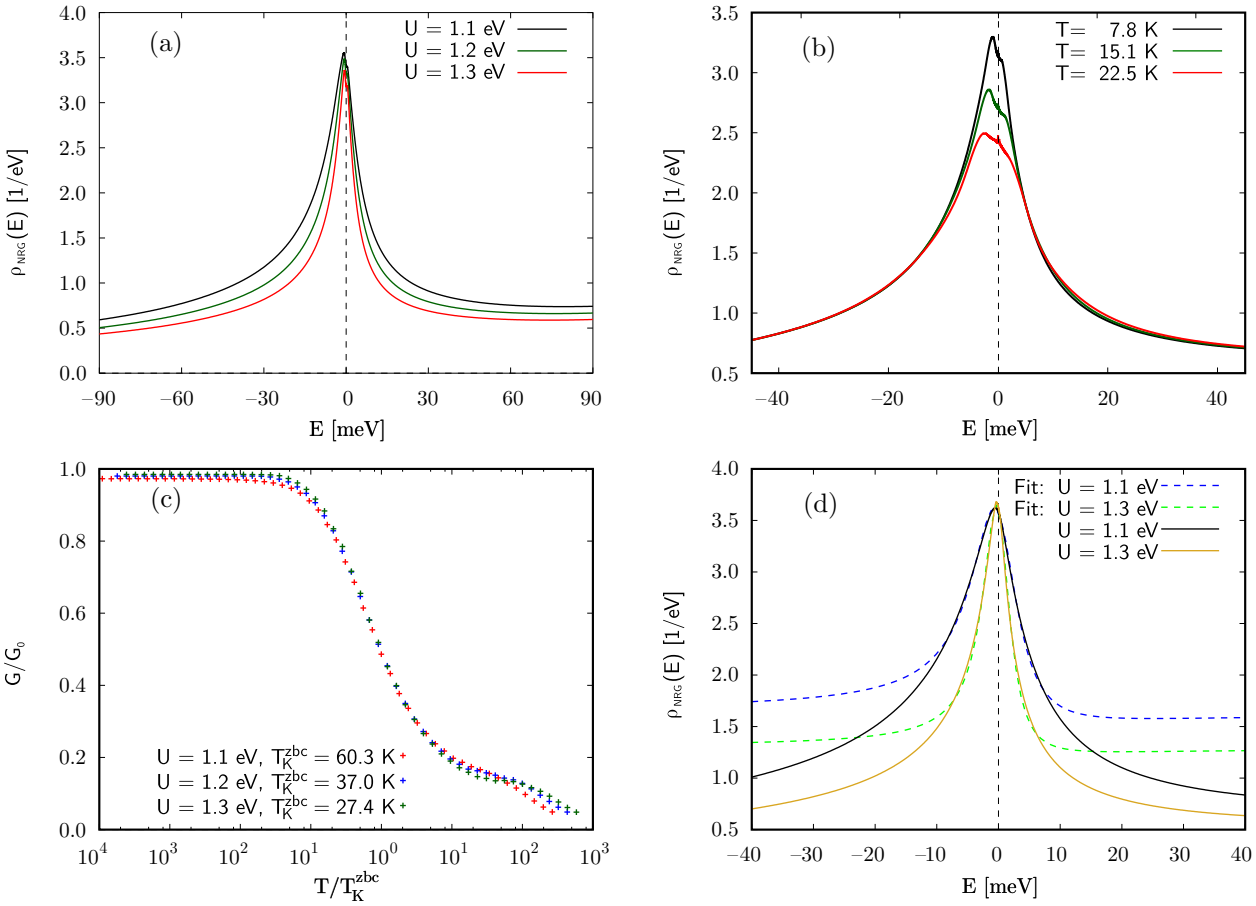

FIG. 13. (Color online) Results of the NRG calculations based on the LDA+GdW for the Au-PTCDA complex on Au(111). (a) Spectra for three different values $U = 1.1, 1.2, 1.3$ eV and $T = 5$ K. The Kondo temperature is increasing with decreasing U. (b) Spectra for different temperatures for $U = 1.2$ eV. (c) The temperature dependent differential conductance for different interactions U as a universal function of T/T_K^{zbc}. (d) Zero-temperature spectra for the interactions $U = 1.1$ and 1.3 eV and their Fano fits to extract the FWHM. For more details see main text.

for the Kondo temperature of the particle-hole asymmetric Anderson model, in which the same orbital parameters from our *ab initio* DFT/MBPT calculations that are used as input for the NRG enter, but where the full energy-dependent hybridization strength $\Gamma(E)$ is replaced by its value at the Fermi energy, i.e., $\Gamma = \Gamma(0)$. This leads to an analytic estimate of the Kondo temperature which we denote by $T_K(\Gamma, \epsilon_0, U)$. (c) The analysis of the FWHM of the zero-temperature spectral function around the chemical potential (i.e., of the Kondo resonance) provides T_K^{FWHM}.

a. Kondo temperature T_K^{zbc} from zero-bias conductance. Figure 13(b) displays the calculated LDA+GdW+NRG orbital spectral functions $\rho_{NRG}(E)$ for the LUMO+Au orbital at fixed $U = 1.2$ eV and at three different temperatures. The spectra are in a good agreement with the corresponding experimental results for the differential conductance $dI/dV(V)$ as depicted in Fig. 7(d), with the exception of the peak asymmetry, see below. The temperature dependent spectral function $\rho_{NRG}(E)$ enters the calculation of the differential conductance [43,44] in the tunneling regime,

$$\frac{dI}{dV}(V) = G_0 \int dE\, \pi\Gamma(E)\rho_{NRG}(E)(-f'_{tip}(E,V)), \quad (8)$$

where the reference conductance G_0 is given by [43]

$$G_0 = \frac{2e^2}{h}\frac{4\Gamma_{tip}(0)\Gamma(0)}{(\Gamma_{tip}(0)+\Gamma(0))^2}. \quad (9)$$

Note that G_0 depends only on $\Gamma(0)$ and $\Gamma_{tip}(0)$, the charge fluctuation scales at the chemical potential, induced by the coupling to the substrate and the tip, respectively. $f_{tip}(E,V)$ denotes the Fermi function of the STM tip and also includes the bias voltage V. For an STM tunneling contact, $\Gamma_{tip}(0) \to 0$, hence $G_0 \to (2e^2/h)(4\Gamma_{tip}(0)/\Gamma(0))$ and the tunnel current is strongly suppressed. For low temperatures, $-f'_{tip}(E,V) \to \delta(E - eV)$ and $dI/dV(V)$ becomes $\pi G_0 \Gamma(eV)\rho_{NRG}(eV)$.

Fitting the zero-bias conductance, Eq. (8), obtained from our LDA+GdW+NRG calculation with Eq. (6) yields Kondo temperatures ranging from $T_K^{zbc} = 27.4$ K for $U = 1.3$ eV to $T_K^{zbc} = 60.3$ K for $U = 1.1$ eV. These values are perfectly bracketing the experimentally estimated Kondo temperature of $T_K^{exp,zbc} = (38 \pm 8)$ K, and the best agreement with the experimental fit in Fig. 7(c) requires $U = 1.2$ eV, for which we obtain $T_K^{zbc} = 37.0$ K (Table III). In Fig. 13(c), the calculated differential conductance, normalized to G_0, is shown as a universal function of T/T_K^{zbc}, employing the fitted Kondo temperatures.

TABLE III. Experimental and calculated Kondo temperatures in K. For the calculated T_K^{zbc} and T_K^{FWHM} we have used the full energy-dependent $\Gamma(E)$, while for $T_K(\Gamma,\epsilon_0,U)$, Eq. (10) has been evaluated for $\Gamma = \Gamma(0) = 86$ meV. For further details, cf. main text.

		U		
	Exp.	1.1 eV	1.2 eV	1.3 eV
T_K^{zbc}	38 ± 8	60.3	37.0	27.4
$T_K(\Gamma,\epsilon_0,U)$	n/a	41.7	28.4	19.5
T_K^{FWHM}	30.7 ± 1	51.0	42.9	30.2

b. Analytic Kondo temperature $T_K(\Gamma,\epsilon_0,U)$ from the asymmetric Anderson model. In general, the Kondo temperature is defined as the universal energy scale governing the excitation and the thermodynamic response at low temperatures. Physical properties, however, also depend on the degree of particle-hole symmetry breaking. This degree enters (i) not only the analytic expression for T_K and (ii) governs the asymmetric shape of the spectral function [see Figs. 13(a), 13(b), and 13(d)] and, therefore, (iii) is also responsible for the asymmetric dI/dV at small bias voltages.

Krishna-murthy *et al.* [40] have shown that the Kondo temperature of the asymmetric Anderson model with a constant hybridization function $\Gamma(E) = \text{const.}$ is given by

$$T_K(\Gamma,\epsilon_0,U) = 0.182|E_0^*|\sqrt{\rho J_{\text{eff}}}\exp\left(-\frac{1}{\rho J_{\text{eff}}}\right) \quad (10)$$

for the regime where double occupation is energetically suppressed and the orbital remains close to integer valence. E_0^* is the self-consistent solution of $E_0^* = \epsilon_0 + (\Gamma/\pi)\ln(-U/E_0^*)$, describing the renormalization of the bare level due to high-energy charge fluctuations. $\rho J_{\text{eff}} = \rho J[1 + (\pi\rho K)^2]^{-1}$ contains not only the dimensionless Kondo coupling

$$\rho J = \frac{2\Gamma}{\pi}\left(\frac{1}{|E_0^*|} + \frac{1}{\epsilon_0 + U}\right), \quad (11)$$

but also a modification by the degree of particle-hole symmetry breaking

$$\rho K = \frac{\Gamma}{2\pi}\left(\frac{1}{|E_0^*|} - \frac{1}{\epsilon_0 + U}\right), \quad (12)$$

both obtained from the Schrieffer-Wolff transformation [45]. At particle-hole symmetry, ρK vanishes, and for weak coupling $E_0^* \approx \epsilon_0$.

Since the Kondo effect is dominated by the low-energy excitations, we use in Eq. (10) the value $\Gamma(E = 0) \approx 86$ meV extracted from the energy-dependent hybridization function as provided by the LDA+GdW approach and depicted in Fig. 12. For $U = 1.2$ eV, $\epsilon_0 = -0.95$ eV, and $\Gamma(E = 0) = 86$ meV, we obtain $T_K(\Gamma,\epsilon_0,U) = 28.4$ K, which agrees well with the numerical fit to the differential conductance presented in Fig. 13(c) ($T_K^{zbc} = 37.0$ K for $U = 1.2$ eV). The $T_K(\Gamma,\epsilon_0,U)$ for the other values of U can be found in Table III.

When obtaining T_K^{zbc} from the temperature dependence of the LDA+GdW+NRG zero-bias conductance, we found that a decreasing U yields an increasing Kondo temperature. This behavior can be analytically understood with the exponential dependence of T_K on ρJ, the latter given by Eq. (11). T_K has a minimum at particle-hole symmetry $\epsilon_0 = -U/2$ and two maxima, one at $\epsilon_0 = 0$ and the second at $\epsilon_0 = -U$. In the present case, with decreasing U, we move further away from the particle-hole symmetric point towards the mixed valence regime where $\epsilon_0 \approx -U$ and, therefore, the Kondo temperature is rising.

We have to bear in mind, however, that this analytical Kondo temperature neglects effects stemming from the energy dependency of $\Gamma(E)$. Therefore $T_K(\Gamma,\epsilon_0,U)$ can only serve as a preliminary estimate, needing modification by our full LDA+GdW+NRG approach for modeling of the experiment.

c. Kondo temperature T_K^{FWHM} from the width of the Kondo peak in the zero-temperature spectral function. Using Eq. (5), the Kondo temperature has been extracted from the experimental data [Fig. 7(a)]. We now apply the same procedure to the LDA+GdW+NRG data in Fig. 13(a). The result is shown in Fig. 13(d).

Since the NRG is able to reach arbitrarily small temperatures, a temperature dependent fit is not required, and Eq. (5) simplifies to

$$\text{FWHM}(T = 0) = 2k_B T_K^{FWHM}. \quad (13)$$

Furthermore, $dI/dV(V) \propto \rho(E = eV)$ in the tunneling regime for $T \to 0$, and T_K^{FWHM} can be estimated directly from the spectral function. However, away from particle-hole symmetry, the spectra and, therefore, the dI/dV curves are asymmetric. It is apparent in Fig. 13(a) that at energies $|E| > k_B T_K$ the spectra are modified by the charge scattering term ρK, as defined in Eq. (12). Given this asymmetry, three questions arise, namely (i) how to extract T_K^{FWHM}, (ii) do the different fit procedures yield comparable values, and (iii) how do the various T_K^{FWHM} compare with the other estimates of the Kondo temperature, namely T_K^{zbc} and $T_K(\Gamma,\epsilon_0,U)$?

The simplest approach would be to take the definition for the full width at half maximum (FWHM) literally. However, in addition to the Kondo peak, the spectra also contain broad charge-excitation peaks at higher energies that invalidate such a procedure. Due to this background, the estimates of T_K^{FWHM} are typically double the value of those obtained by the fit function (6).

To allow for an asymmetry [46,47] in the fitting process, we employ here a Fano-resonance line shape of the form $\rho(E) = \rho_0 + A\frac{(q+\epsilon)^2}{1+\epsilon^2}$ with $\epsilon = (E - E_0)/\Gamma$ for the Kondo peak to extract its FWHM. E_0 determines the location of the resonance, which is shifted slightly away from the chemical potential in accordance with the Friedel sum rule [48]. While q parametrizes the asymmetry of the spectrum, the width Γ defines the fit for T_K^{FWHM}. Figure 13(d) shows the zero-temperature spectra for two different interactions, $U = 1.1$ and 1.3 eV, and the corresponding Fano fits. Depending on the interaction U, we find Kondo temperatures extracted from our NRG spectra ranging from $T_K^{FWHM} = 30.2$ to 51.0 K (Table III), which again brackets the measured $T_K^{exp,FWHM} = (30.7 \pm 1.0)$ K.

We stress again that when using Eq. (5) in highly particle-hole asymmetric cases, one should bear in mind that the extracted T_K^{FWHM} depends on the fitted function, which requires significant modifications from a symmetric Lorentzian. Furthermore, as we show in the next paragraph,

TABLE IV. Experimental and calculated Kondo temperatures in K, here for a constant $\Gamma = 86$ meV. For details, cf. Sec. III D 3.

		U		
	Exp.	1.1 eV	1.2 eV	1.3 eV
T_K^{zbc}	38 ± 8	98.0	63.0	42.8
$T_K(\Gamma,\epsilon_0,U)$	n/a	41.7	28.4	19.5
T_K^{FWHM}	30.7 ± 1.0	74.8	57.0	42.9
T_K^{μ}	n/a	49.9	34.2	23.9
$T_K(\Gamma,\epsilon_0,U)/T_K^{\mu}$	–	0.836	0.830	0.810
$T_K(\Gamma,\epsilon_0,U)/T_K^{zbc}$	–	0.426	0.450	0.456
$T_K(\Gamma,\epsilon_0,U)/T_K^{FWHM}$	–	0.577	0.498	0.455

T_K^{FWHM} can only give the correct order of magnitude of the Kondo temperature, since its value is definition-dependent and does not need to coincide with the Kondo temperature defined in Eq. (10) that has been derived from the screening of the local spin moment. We have summarized the experimentally obtained and the calculated Kondo temperatures in Table III.

3. Comparison of Kondo temperatures

We now turn to a comparison of the various calculated Kondo temperatures among each other in order to provide a guideline for a reliable extraction of T_K from the experiment. In Sec. III B, we have extracted experimental Kondo temperatures from the FWHM of the spectral function, Eq. (5) and Fig. 7(a), and from the zero-bias conductance using the fit function Eq. (6) [see Fig. 7(c)]. Since the Kondo temperature is only a crossover scale, it is only defined up to an arbitrary constant of the order one. The question arises whether $T_K^{exp,zbc}$ and $T_K^{exp,FWHM}$ should indeed be expected to be identical *up to a universal scaling constant*.

The NRG provides optimal tools to systematically investigate the difference between the various definitions of the Kondo scale. In order to exclude an influence of the energy dependent hybridization function on this comparison, we have repeated the NRG calculations with a constant $\Gamma = 86$ meV and extracted new values of T_K^{zbc} and T_K^{FWHM} from these calculations. These new values, which can now be directly compared to the analytic estimate $T_K(\Gamma,\epsilon_0,U)$, are summarized in the upper part of Table IV. The table also contains values for T_K^{μ}, determined again for constant $\Gamma = 86$ meV. Wilson [40,41] has defined the Kondo temperature as the temperature T_K^{μ} at which the local moment is reduced to approximately 26% of the original value, by screening through the conduction electrons. (At $T = 0$, i.e., in the Kondo singlet ground state, the effective moment is zero.) Hence T_K^{μ} follows from the implicit equation

$$\mu_{eff}^2 = T_K^{\mu}\chi\left(T_K^{\mu}\right) = 0.07, \tag{14}$$

where μ_{eff}^2 is the effective local magnetic moment and $\chi(T)$ its isothermal magnetic susceptibility. Note that this screening has also entered the analytical estimate $T_K(\Gamma,\epsilon_0,U)$ in Eq. (10) in Sec. III D 2 b.

Calculating the ratios $T_K(\Gamma,\epsilon_0,U)/T_K^{\mu}$ and $T_K(\Gamma,\epsilon_0,U)/T_K^{zbc}$ for each of the three different values of $U = 1.1, 1.2, 1.3$ eV, corresponding to $E_0 = -0.88, -0.95, -1.02$ eV, we found nearly constant ratios $T_K(\Gamma,\epsilon_0,U)/T_K^{\mu} \approx 0.83$ and $T_K(\Gamma,\epsilon_0,U)/T_K^{zbc} \approx 0.45$. Consequently, all three definitions T_K^{μ}, $T_K(\Gamma,\epsilon_0,U)$ and T_K^{zbc} are fully equivalent and connected by universal scaling factors.

This should be contrasted with the situation regarding T_K^{FWHM}; Table IV shows that the ratios $T_K(\Gamma,\epsilon_0,U)/T_K^{FWHM}$ are *not* constant and U dependent, varying over a range from $\approx$0.58 to $\approx$0.46. This state of affairs does not change if the fitting procedure of the zero-bias conductance peak is changed. In particular, we tested three different procedures: (i) a Lorentz-fit to the symmetrized spectrum $\rho_{sym}(\omega) = 0.5(\rho(\omega) + \rho(-\omega))$, (ii) a Lorentz-fit to the low-energy part of the spectrum, and (iii) a fit using the Fano line shape as described above. All three fitting procedures yield roughly the same estimate for T_K^{FWHM}. We therefore conclude that the scale T_K^{FWHM} is nonuniversal and depends on the degree of particle-hole symmetry breaking. In particular, for small U, we find a T_K^{FWHM} that is smaller than the fit to the zero-bias conductance, while it approaches T_K^{zbc} for $U = 1.3$ eV where the spectrum is narrower and significantly more symmetric.

The above discussion shows that the difference between $T_K^{exp,zbc}$ and $T_K^{exp,FWHM}$ is due a nonuniversal scaling constant. Therefore, the most reliable way of extracting T_K from experiments remains the fit of the temperature-dependent zero-bias conductance (T_K^{zbc}), since at any temperature only excitations of the order of T enter, while T_K^{FWHM} measured at $T/T_K \ll 1$ always contains high-energy excitations in addition to errors stemming from nonequilibrium effects due to the finite current through the molecule. However, Table IV shows that T_K^{FWHM} can still serve as a reasonable estimate for T_K, providing the correct order of magnitude of the Kondo temperature.

It is interesting to note that the Kondo temperatures calculated with a constant Γ and listed in Table IV are significantly different from those obtained with the energy dependent $\Gamma(E)$, which turned out to match the experimental findings very well. The Kondo temperatures at constant Γ exceed the ones for nonconstant $\Gamma(E)$ by up to a factor of two. We can thus conclude that a combined full LDA+GdW+NRG approach is needed to explain the experimental data on a quantitative level. In particular, we achieve a perfect match between experiment ($T_K^{exp,zbc} \approx 38$ K) and theory ($T_K^{zbc} = 37$ K) for $U = 1.2$ eV, which is in the center of the range of U parameters calculated from DFT/MBPT using Eq. (4).

4. LUMO+Au orbital occupancy n

The NRG also provides information on the occupancy of the local LUMO+Au orbital. While the LDA+GdW predicts an occupancy of $n = 0.71$, the inclusion of correlation effects by the NRG reduces this value to $n = 0.55$. Such a reduction is expected, since the Coulomb repulsion strongly suppresses double occupancy of the orbital and thus constrains the filling much closer to half-integer values (note that in our definition a completely occupied orbital with two electrons of opposite spin has $n = 1$). However, the LDA+GdW and the LDA+GdW+NRG agree in predicting the binding of an extra fraction of an electron that is drawn from the substrate (LDA+GdW+NRG: 0.1 electrons, LDA+GdW: 0.4 electrons), in addition to the one electron from the Au

atom. We note in passing that 0.1 electrons is exactly the difference of occupation between Au-PTCDA and PTCDA on the Au(111) surface within LDA.

Furthermore, it is interesting to note in this context that in comparison to the LDA+GdW the LSDA+GdW occupation ($n_{\mathrm{LSDA+GdW}} = 0.50$) is closer to that of NRG ($n = 0.55$). As expected, this is coupled to a lower U derived from the LSDA+GdW ($U = 1.1$ eV) than from the LSDA+GdW ($U = 1.3$ eV). However, as argued above, the reduction of the occupancy in the LSDA+GdW is not occurring for the correct physical reason.

IV. SUMMARY AND CONCLUSION

In this work, we have shown that when doping a PTCDA/Au(111) monolayer with single Au atoms, Au-PTCDA complexes are formed by a spontaneous chemical reaction. A DFT calculation reveals that the Au-PTCDA complex is also stable in the gas phase. Due to an unpaired electron, drawn from the Au 6s orbital, this complex is a paramagnetic radical ($S = \frac{1}{2}$). Remarkably, the orbital in which the unpaired spin resides extends over the whole molecule and is related to the LUMO of free PTCDA. Specifically, it is the bonding combination of the Au 6s orbital and the LUMO of PTCDA. The split between bonding and antibonding orbitals in the gas phase complex amounts to approximately 1 eV if calculated at LDA level.

On the Au(111) surface, an additional small fraction of an electron (about 0.1 electrons) is drawn from the substrate into the bonding orbital of the Au-PTCDA complex. However, this additional charge transfer is effectively limited by a rather strong intraorbital Coulomb repulsion U. In fact, the bonding LUMO+Au orbital remains close to a singly occupied orbital. In this sense, the Au-PTCDA complex on Au(111) is intermediate between PTCDA on Au(111), where no charge transfer takes place [19], and PTCDA on Ag(111), where nearly two electrons are transferred from the metal surface to the molecule [49]. Apparently, the coupling between adsorbate and substrate is much weaker in the case of Au-PTCDA/Au(111) than in PTCDA/Ag(111), such that in spite of similar intraorbital repulsions double occupancy is only suppressed for Au-PTCDA/Au(111). On the other hand, comparing Au-PTCDA/Au(111) to PTCDA/Au(111), where the LUMO remains unfilled, we see that the charge transfer from the Au atom to the π system bypasses the charging barrier for PTCDA on Au(111) that is caused by the large work function of Au(111).

As a result of the restriction to single occupancy, the spin degree of freedom of the complex is retained when it is adsorbed on the Au(111) surface. The thus stabilized spin of the complex interacts with conduction electrons of the metal surface. As a consequence, the Kondo effect unfolds in this system. In our experimental STS spectra, it reveals itself by the sharp resonance in the single-particle spectral function at the chemical potential. Analyzing both the width (FWHM) and the height (zero-bias conductance) of this resonance as a function of temperature, we find a behavior that is consistent with the predicted temperature dependence of Kondo resonances, yielding Kondo temperatures of $\approx$38 K from the zero-bias conductance and $\approx$31 K from the FWHM, respectively. The observation of the Kondo effect in the present system is the unambiguous proof that the Au-PTCDA complex is indeed a paramagnetic radical with $S = \frac{1}{2}$.

On the theory side, we have a achieved a fully quantitative description of the Au-PTCDA complex, by applying a hierarchy of methods, employing density functional theory in the local density and generalized gradient approximations, including van der Waals corrections, as well many-body perturbation theory in the GW and LDA+GdW approximations, and the numerical renormalization group approach.

As far as geometric structure is concerned, the "adsorption site" found by theory, i.e., the site at which the reaction between the Au atom on the PTCDA molecule occurs, is in agreement with experiment. This means that the chemical structure of the complex is correctly predicted. Moreover, STM simulations allow the identification of some of the experimentally observed complexes as being contaminated by an adsorbed hydrogen molecule.

Electronic structure calculations for the gas-phase complex show the importance of quasiparticle corrections for predicting the correct excitation spectrum. These increase the gap to approximately 3 eV. This large gap is, however, reduced again to approximately 1 eV for the adsorbed complex (in an ordered monolayer structure), due to screening by the metal substrate and neighboring PTCDA molecules of the Au-PTCDA complexes, in good agreement with experiment. To predict the full excitation spectrum correctly, including the low-energy region that is shaped by the spin degree of freedom, we have applied the numerical renormalization group approach, mapping the MBPT result on the $S = \frac{1}{2}$ single-impurity Anderson Hamiltonian. Notably, in doing so, we take the full energy dependence of the coupling function into account, a fact that turns out to be crucial for the quantitatively correct description of the system.

The NRG yields the spectrum of the Au-PTCDA complex on the Au(111) surface. It consists of two charge excitation peaks, one below and the other above the chemical potential, both within 0.25 eV of the corresponding experimental values, and the Kondo resonance at the Fermi energy as the third feature. Due to the particle-hole asymmetry of the given system, the calculated Kondo resonance acquires an asymmetric line shape. In experiment, however, the asymmetry of the Kondo peak is less obvious, although the charge excitations peaks clearly show the particle-hole asymmetry also in the measured spectra.

In order to provide a guideline how the Kondo temperature can be extracted reliably from experiment for the present system and for particle-hole asymmetric systems in general, we have carried out a careful analysis of the scaling behavior of various definitions of the Kondo temperature T_{K}. Because the Kondo temperature defines a crossover scale, Kondo temperatures that are extracted from an experiment or an NRG calculation may vary up to a scaling factor. However, for valid extraction schemes, this scaling factor must be universal. If the scaling factor turns out to be nonuniversal in the sense that it depends on parameters of the model, the extraction scheme is inadequate.

In the present system, we find that Kondo temperatures extracted from the temperature dependence of both the zero-bias conductance and the local moment screening scale universally

with the analytic formula for the particle-hole asymmetric Anderson model, while the Kondo temperature derived from the FWHM of the zero-bias peak scales nonuniversally, no matter how the FWHM is determined. For the experiment, this means that we need to use the zero-bias conductance to obtain a Kondo temperature that is not prejudiced by nonuniversal aspects of the line shape. Applying this procedure to experiment and NRG, we obtain Kondo temperatures between 60 and 27 K for U in the range 1.1 to 1.3 eV. This allows us to narrow down possible U values from the range calculated in DFT/MBPT to around $U = 1.2$ eV, since only for this value the NRG yields a Kondo temperature ($T_K = 37$ K) close to experiment ($T_K \approx 38$ K). The other case where experiment and theory agree, namely, 30.7 versus 30.2 K for the "Kondo temperature" derived from the width of the zero-bias conductance, can be discarded as coincidental, because this extracted parameter is nonuniversal and therefore not a good Kondo scale. Finally, we note that in spite of the fact that the Kondo effect is determined by low-energy excitation around the chemical potential, the replacement of the coupling function $\Gamma(E)$ by its value $\Gamma(0)$ at the Fermi energy is not sufficient. In the present case, this incurs an error of nearly a factor of 2 in the Kondo temperatures. Using the full energy dependence of the coupling function is therefore mandatory, if an accurate quantitative description of the system is sought.

Finally, we stress that the delocalized character of the spin-carrying π orbital makes the Au-PTCDA complex an interesting system in the investigation of spin phenomena and especially in the study of interactions between "magnetic molecules." Because the Kondo temperature depends very sensitively on molecule-metal coupling, energy-level position, and Coulomb interaction, the good agreement between experiment and theory, which we report here, proves that these parameters and, more generally, the structural and electronic properties of the Au-PTCDA complex are accurately described by DFT/MBPT. The possibility to predict the properties of a single complex accurately promises this system to be an ideal candidate for the quantitative study of interactions between extended molecular magnets.

ACKNOWLEDGMENTS

Two of us (BL and FBA) have received support by the Deutsche Forschungsgemeinschaft through AN 275/7-1 and support from the NIC Jülich for CPU time under project no. HHB00.

[1] M. N. Leuenberger and D. Loss, Quantum computing in molecular magnets, Nature (London) **410**, 789 (2001).

[2] G. D. Scott and D. Natelson, Kondo resonances in molecular devices, ACS Nano **4**, 3560 (2010).

[3] D. Gatteschi, R. Sessoli, and J. Villain, *Molecular Nanomagnets* (Oxford University Press, Oxford, 2006).

[4] I. Fernández-Torrente, D. Kreikemeyer-Lorenzo, A. Stróżecka, K. J. Franke, and J. I. Pascual, Gating the charge state of single molecules by local electric fields, Phys. Rev. Lett. **108**, 036801 (2012).

[5] R. Temirov, A. Lassise, F. B. Anders, and F. S. Tautz, Kondo effect by controlled cleavage of a single-molecule contact, Nanotechnol. **19**, 065401 (2008).

[6] C. Toher, R. Temirov, A. Greuling, F. Pump, M. Kaczmarski, M. Rohlfing, G. Cuniberti, and F. S. Tautz, Electrical transport through a mechanically gated molecular wire, Phys. Rev. B **83**, 155402 (2011).

[7] A. Greuling, R. Temirov, B. Lechtenberg, F. B. Anders, M. Rohlfing, and F. S. Tautz, Spectral properties of a molecular wire in the Kondo regime, Physica Status Solidi (b) **250**, 2386 (2013).

[8] A. Greuling, M. Rohlfing, R. Temirov, F. S. Tautz, and F. B. Anders, *Ab initio* study of a mechanically gated molecule: From weak to strong correlation, Phys. Rev. B **84**, 125413 (2011).

[9] L. Liu, K. Yang, Y. Jiang, B. Song, W. Xiao, L. Li, H. Zhou, Y. Wang, S. Du, M. Ouyang, W. A. Hofer, A. H. Castro Neto, and H.-J. Gao, Reversible single spin control of individual magnetic molecule by hydrogen atom adsorption, Sci. Rep. **3**, 1210 (2013).

[10] B. W. Heinrich, G. Ahmadi, V. L. Müller, L. Braun, J. I. Pascual, and K. J. Franke, Change of the magnetic coupling of a metal–organic complex with the substrate by a stepwise ligand reaction, Nano Lett. **13**, 4840 (2013).

[11] C. Krull, R. Robles, A. Mugarza, and P. Gambardella, Site- and orbital-dependent charge donation and spin manipulation in electron-doped metal phthalocyanines, Nat. Mater. **12**, 337 (2013).

[12] F. Mohn, J. Repp, L. Gross, G. Meyer, M. S. Dyer, and M. Persson, Reversible bond formation in a gold-atom organic-molecule complex as a molecular switch, Phys. Rev. Lett. **105**, 266102 (2010).

[13] J. Kröger, L. Limot, H. Jensen, R. Berndt, S. Crampin, and E. Pehlke, Surface state electron dynamics of clean and adsorbate-covered metal surfaces studied with the scanning tunnelling microscope, Prog. Surf. Sci. **80**, 26 (2005).

[14] We are using version 3.2 of the SIESTA, which is available at http://departments.icmab.es/leem/siesta.

[15] P. Ordejón, E. Artacho, and J. M. Soler, Self-consistent order-*N* density-functional calculations for very large systems, Phys. Rev. B **53**, R10441 (1996).

[16] J. M. Soler, E. Artacho, J. D. Gale, A. García, J. Junquera, P. Ordejón, and D. Sánchez-Portal, The SIESTA method for *ab initio* order-*N* materials simulation, J. Phys.: Condens. Matter **14**, 2745 (2002).

[17] J. P. Perdew, K. Burke, and M. Ernzerhof, Generalized gradient approximation made simple, Phys. Rev. Lett. **77**, 3865 (1996).

[18] V. G. Ruiz, W. Liu, E. Zojer, M. Scheffler, and A. Tkatchenko, Density-functional theory with screened van der waals interactions for the modeling of hybrid inorganic-organic systems, Phys. Rev. Lett. **108**, 146103 (2012).

[19] S. K. M. Henze, O. Bauer, T.-L. Lee, M. Sokolowski, and F. S. Tautz, Vertical bonding distances of PTCDA on Au(111) and Ag(111): Relation to the bonding type, Surf. Sci. **601**, 1566 (2007).

[20] T. Ogawa, K. Kuwamoto, S. Isoda, T. Kobayashi, and N. Karl, 3,4:9,10-Perylenetetracarboxylic dianhydride (PTCDA)

by electron crystallography, Acta Crystallograph. Sec. B **55**, 123 (1999).

[21] J. Tersoff and D. R. Hamann, Theory of the scanning tunneling microscope, Phys. Rev. B **31**, 805 (1985).

[22] T. Deilmann, P. Krüger, M. Rohlfing, and D. Wegner, Adsorption and STM imaging of tetracyanoethylene on Ag(001): An *ab initio* study, Phys. Rev. B **89**, 045405 (2014).

[23] L. Hedin, New method for calculating the one-particle Green's function with application to the electron-gas problem, Phys. Rev. **139**, A796 (1965).

[24] M. Rohlfing, Electronic excitations from a perturbative LDA+GdW approach, Phys. Rev. B **82**, 205127 (2010).

[25] M. Rohlfing, P. Krüger, and J. Pollmann, Quasiparticle band-structure calculations for C, Si, Ge, GaAs, and SiC using Gaussian-orbital basis sets, Phys. Rev. B **48**, 17791 (1993).

[26] J. Wieferink, P. Krüger, and J. Pollmann, Improved hybrid algorithm with Gaussian basis sets and plane waves: First-principles calculations of ethylene adsorption on ß-SiC(001)-(3×2), Phys. Rev. B **74**, 205311 (2006).

[27] W. H. A. Thijssen, D. Djukic, A. Otte, R. H. Bremmer, and J. M. van Ruitenbeek, Vibrationally induced two-level systems in single-molecule junctions, Phys. Rev. Lett. **97**, 226806 (2006).

[28] D. Djukic, K. S. Thygesen, C. Untiedt, R. H. M. Smit, K. W. Jacobsen, and J. M. van Ruitenbeek, Stretching dependence of the vibration modes of a single-molecule Pt–H_2–Pt bridge, Phys. Rev. B **71**, 161402 (2005).

[29] K. Svensson, L. Bengtsson, J. Bellman, M. Hassel, M. Persson, and S. Andersson, Two-Dimensional quantum rotation of adsorbed H_2, Phys. Rev. Lett. **83**, 124 (1999).

[30] L. Bengtsson, K. Svensson, M. Hassel, J. Bellman, M. Persson, and S. Andersson, H_2 adsorbed in a two-dimensional quantum rotor state on a stepped copper surface, Phys. Rev. B **61**, 16921 (2000).

[31] S. Li, A. Yu, F. Toledo, Z. Han, H. Wang, H. Y. He, R. Wu, and W. Ho, Rotational and vibrational excitations of a hydrogen molecule trapped within a nanocavity of tunable dimension, Phys. Rev. Lett. **111**, 146102 (2013).

[32] F. D. Natterer, F. Patthey, and H. Brune, Distinction of nuclear spin states with the scanning tunneling microscope, Phys. Rev. Lett. **111**, 175303 (2013).

[33] F. D. Natterer, F. Patthey, and H. Brune, Resonant-enhanced spectroscopy of molecular rotations with a scanning tunneling microscope, ACS Nano **8**, 7099 (2014).

[34] K. Nagaoka, T. Jamneala, M. Grobis, and M. F. Crommie, Temperature dependence of a single Kondo impurity, Phys. Rev. Lett. **88**, 077205 (2002).

[35] J. Lambe and R. C. Jaklevic, Molecular vibration spectra by inelastic electron tunneling, Phys. Rev. **165**, 821 (1968).

[36] D. Goldhaber-Gordon, J. Göres, M. A. Kastner, H. Shtrikman, D. Mahalu, and U. Meirav, From the Kondo regime to the mixed-valence regime in a single-electron transistor, Phys. Rev. Lett. **81**, 5225 (1998).

[37] N. Dori, M. Menon, L. Kilian, M. Sokolowski, L. Kronik, and E. Umbach, Valence electronic structure of gas-phase 3,4,9,10-perylene tetracarboxylic acid dianhydride: Experiment and theory, Phys. Rev. B **73**, 195208 (2006).

[38] According to the Mermin Wagner Theorem [51], it is unphysical to obtain a spin-polarized solution in a single orbital as the ground state of a system without an internal or external magnetic field in less than three dimensions. Quantum fluctuations will always lead to an unpolarised state with lower energy. Therefore, in the real system the spin-dependent single particle densities of state must be degenerate and the local magnetic moment is created by the (intraorbital) Coulomb repulsion that induces a dynamical correlation between the single particle densities of both spin channels and that therefore cannot be modelled as an effective single particle potential.

[39] S. Duhm, A. Gerlach, I. Salzmann, B. Bröker, R. Johnson, F. Schreiber, and N. Koch, PTCDA on Au(111), Ag(111) and Cu(111): Correlation of interface charge transfer to bonding distance, Org. Electron. **9**, 111 (2008).

[40] H. R. Krishna-murthy, J. W. Wilkins, and K. G. Wilson, Renormalization-group approach to the Anderson model of dilute magnetic alloys. II. Static properties for the asymmetric case, Phys. Rev. B **21**, 1003 (1980); **21**, 1044 (1980).

[41] R. Bulla, T. A. Costi, and T. Pruschke, Numerical renormalization group method for quantum impurity systems, Rev. Mod. Phys. **80**, 395 (2008).

[42] M. T. Glossop and D. E. Logan, Single-particle dynamics of the Anderson model: A local moment approach, J. Phys.: Condens. Matter **14**, 6737 (2002).

[43] Y. Meir and N. S. Wingreen, Landauer formula for the current through an interacting electron region, Phys. Rev. Lett. **68**, 2512 (1992).

[44] A. Schiller and S. Hershfield, Theory of scanning tunneling spectroscopy of a magnetic adatom on a metallic surface, Phys. Rev. B **61**, 9036 (2000).

[45] J. R. Schrieffer and P. A. Wolff, Relation between the Anderson and Kondo Hamiltonians, Phys. Rev. **149**, 491 (1966).

[46] L. Merker, S. Kirchner, E. Muñoz, and T. A. Costi, Conductance scaling in Kondo-correlated quantum dots: Role of level asymmetry and charging energy, Phys. Rev. B **87**, 165132 (2013).

[47] E. Muñoz, C. J. Bolech, and S. Kirchner, Universal out-of-equilibrium transport in Kondo-correlated quantum dots: Renormalized Dual fermions on the keldysh contour, Phys. Rev. Lett. **110**, 016601 (2013).

[48] D. C. Langreth, Friedel sum rule for Anderson's model of localized impurity states, Phys. Rev. **150**, 516 (1966); F. B. Anders, N. Grewe, and A. Lorek, On the validity of sum rules and Fermi-liquid properties in calculations for strongly correlated electrons, Z. Phys. B Condens. Matter **83**, 75 (1991).

[49] M. Rohlfing, R. Temirov, and F. S. Tautz, Adsorption structure and scanning tunneling data of a prototype organic-inorganic interface: PTCDA on Ag(111), Phys. Rev. B **76**, 115421 (2007).

[50] N. Takeuchi, C. T. Chan, and K. M. Ho, Au(111): A theoretical study of the surface reconstruction and the surface electronic structure, Phys. Rev. B **43**, 13899 (1991).

[51] N. Mermin and H. Wagner, Absence of ferromagnetism or antiferromagnetism in one- or two-dimensional isotropic Heisenberg models, Phys. Rev. Lett. **17**, 1133 (1966).